



MAX PLANCK INSTITUTE FOR POLYMER RESEARCH  
MOLECULAR SPECTROSCOPY DEPARTMENT

-

JOHANNES GUTENBERG-UNIVERSITÄT MAINZ  
2019

---

**Electrochemical design of a bimetallic  
model surface for EC-TERS studies of  
catalyzed oxidation reactions**

---

**Master's Thesis**

in Chemistry

written by

**DANIEL OHM**

born in Rüdesheim am Rhein

Die vorliegende Arbeit wurde in der Zeit vom 01. Februar 2019 bis zum 31. Juli 2019 im Department für Molekulare Spektroskopie des Max Planck-Instituts für Polymerforschung in Mainz unter Anleitung von Dr. Katrin F. Domke angefertigt.

The presented work was completed from February 1st until July 31st, 2019 in the Molecular Spectroscopy Department of the Max Planck Institute for Polymer Research in Mainz under the supervision of Dr. Katrin F. Domke.

Hiermit versichere ich, dass ich meine Masterarbeit selbstständig verfasst und keine anderen als die angegebenen schriftlichen und elektronischen Quellen sowie andere Hilfsmittel benutzt habe. Alle Ausführungen, die anderen Schriften wörtlich oder sinngemäß entnommen wurden, habe ich kenntlich gemacht.

I hereby confirm that I wrote my master's thesis by myself without using any other written or electronic sources and other tools than stated. All quotations that were made have been indicated.

DANIEL OHM  
(Matrikelnummer: 2681042)

---

*Supervisor/Erstgutachter:*

Dr. Katrin F. Domke

*Second assessor/Zweitgutachter:*

Prof. Dr. Siegfried R. Waldvogel

# Abstract

The design of bimetallic model surfaces was shown in this work. Pd and Ir islands were deposited on Au(111) surfaces using copper underpotential deposition (CuUPD) and subsequent metal displacement to replace copper with Pd and Ir, respectively. The bimetal surfaces were characterized in terms of their activity for hydrogen evolution reaction (HER), oxygen reduction reaction (ORR) and formic acid oxidation catalysis. The island dimensions were varied by changing deposition potential and deposition time during CuUPD experiments to obtain information about the influence of Pd/Au(111) and Ir/Au(111) interfaces on the catalytic activity in subsequent HER, ORR and formic acid oxidation experiments.

The influence of deposition potential and deposition time on the island dimension and size could be shown with scanning tunneling microscopy. The influence of surface coverage on the catalytic activity of the substrates for HER and ORR could be shown by cyclic voltammetry (CV).

# Zusammenfassung

In der vorliegenden Arbeit wurden bimetallische Modelloberflächen designt. Dazu wurden mittels Kupfer Unterpotentialabscheidung (CuUPD) und Austausch von Kupfer durch Palladium bzw. Iridium Inseln auf einer Au(111) abgeschieden und hinsichtlich ihrer Aktivität gegenüber Reaktionen, die von technischer Relevanz in der Entwicklung von Brennstoffzellen sind, untersucht. Die untersuchten Reaktionen waren Wasserstoff-Entwicklung (HER), Sauerstoff Reduktion (ORR) und Ameisensäure Oxidation. Die Dimensionen der Inseln sowie deren Verteilung auf der Oberfläche wurden zur Untersuchung des Einflusses von Pd/Au(111) und Ir/Au(111) Grenzflächen auf die katalytis-

che Aktivität durch Variation von Potential und Abscheidungsdauer während der CuUPD, verändert.

Es konnte der Einfluss von Abscheidungspotential und Abscheidungsdauer während der CuUPD auf die Größe und Verteilung der resultierenden Inseln durch Untersuchungen mit dem Rastertunnelmikroskop gezeigt werden. Der Einfluss der Oberflächenbedeckung auf die katalytische Aktivität der Substrate gegenüber der HER und ORR konnte gezeigt werden.

"Begin at the beginning, [...] and go on  
till you come to the end: then stop."

-Lewis Carroll, *Alice in Wonderland*

# Acknowledgements

I would like to express my great appreciation to **Dr. Katrin F. Domke** for giving me the chance to write my master's thesis in her group, and her valuable suggestions and encouragement during that time. Her ideas and constructive criticism were very much appreciated, as well as the chance to do part of the work at University of Alicante, Spain.

I would like to offer my special thanks to **Jonas H. K. Pfisterer** for his great guidance, assistance in learning EC-TERS and enthusiastic encouragement during my work. He always came up with ideas and help when needed and always had an open ear for any kind of problems that occurred.

My grateful thanks are also extended to **Stephanie Jung**, who helped me with lots of organizational tasks.

I would also like to extend my thanks to the members of the Domke **group**, who helped a lot with discussions and suggestions related to my work and guidance in experiments.

Furthermore I would also like to thank **Prof. Dr. Juan M. Feliu** to offering me the chance to do part of the work of my master's thesis in his lab at the Insitute of Electrochemistry, University of Alicante, Spain. His ideas and suggestions were very useful and much appreciated.

I also wish to acknowledge the help provided by **Valentín Briega Martos** and the rest of the group during my time at University of Alicante.

My special thanks go to my **family** and **friends**, especially mentioned **Sabrina Becker**, for their moral support and help that led to successfully finish this work. They always provided an open ear and distraction when needed and kept me on track.



# Contents

<b>1</b>	<b>Introduction</b>	<b>1</b>
<b>2</b>	<b>Theoretical Fundamentals</b>	<b>3</b>
2.1	Noble-metal surfaces . . . . .	3
2.2	Electrochemical metal deposition and metal displacement . . . . .	5
2.3	Electrocatalysis . . . . .	7
2.4	EC-TERS . . . . .	9
<b>3</b>	<b>Results and Discussion</b>	<b>12</b>
3.1	Choice of a suitable gold substrate . . . . .	12
3.2	CuUPD . . . . .	14
3.3	Systematic study of the influence of different deposition parameters on the size and distribution of the resulting Pd or Ir islands . . . . .	15
3.4	Electrochemical stability of the islands . . . . .	26
3.5	Hydrogen Evolution Reaction (HER) . . . . .	29
3.6	Formic Acid Oxidation . . . . .	33
3.7	Oxygen Reduction Reaction (ORR) . . . . .	36
<b>4</b>	<b>Conclusion and Outlook</b>	<b>40</b>
4.1	Conclusion . . . . .	40
4.2	Outlook . . . . .	41
<b>5</b>	<b>Experimental Methodology</b>	<b>43</b>
5.1	Materials . . . . .	43
5.2	Preparation of the gold-on-glass samples . . . . .	43
5.3	Preparation of the counter and reference electrodes . . . . .	44
5.4	Cyclic Voltammetry measurements . . . . .	45
5.5	CuUPD . . . . .	47
5.6	Metal Displacement . . . . .	47
5.7	Scanning Tunneling Microscopy . . . . .	48

5.8	Electrochemical tip-enhanced Raman spectroscopy . . . . .	48
<b>Bibliography</b>		<b>51</b>
<b>6</b>	<b>Appendix</b>	<b>54</b>
6.1	Pd/Au(111) . . . . .	54
6.1.1	3 s, sweep 0.15 V . . . . .	54
6.1.2	3 s, 0.12 V . . . . .	55
6.1.3	5 s, 0.15 V . . . . .	56
6.1.4	9 s, 0.15 V . . . . .	57
6.1.5	10 s, 0.15 V . . . . .	58
6.2	Ir/Au(111) . . . . .	59
6.2.1	3 s, 0.15 V . . . . .	59
6.2.2	6 s, 0.15 V . . . . .	60
6.2.3	9 s, 0.15 V . . . . .	62
6.2.4	12 s, 0.15 V . . . . .	63
6.3	X-ray photoelectron spectroscopy . . . . .	64
6.3.1	Pd/Au(111) . . . . .	64
6.3.2	Ir/Au(111) . . . . .	66
6.4	Electrochemical cell design . . . . .	68

# List of Abbreviations

<b>AFM</b>	Atomic Force Microscopy
<b>Au</b>	Gold
<b>BCC</b>	Body-Centered Cubic
<b>CCP</b>	Cubic Closest-Packing
<b>CE</b>	Counter Electrode
<b>CuSO<sub>4</sub></b>	Copper Sulphate
<b>CV</b>	Cyclic Voltammetry
<b>EC</b>	Electrochemistry
<b>FCC</b>	Face-Centered Cubic
<b>H<sub>2</sub>IrCl<sub>6</sub></b>	Iridium <sup>IV</sup> Chloride Hydrochloride
<b>H<sub>2</sub>PdCl<sub>4</sub></b>	Palladium <sup>II</sup> Chloride Hydrochloride
<b>H<sub>2</sub>SO<sub>4</sub></b>	Sulphuric Acid
<b>HER</b>	Hydrogen Evolution Reaction
<b>Ir</b>	Iridium
<b>LASER</b>	Light Amplification by Stimulated Emission of Radiation
<b>Milli-Q</b>	Type 1 Ultrapure Water
<b>M</b>	Molarity
<b>MoS<sub>2</sub></b>	Molybdenum Disulfide
<b>ML</b>	Monolayer
<b>OER</b>	Oxygen Evolution Reaction
<b>ORR</b>	Oxygen Reduction Reaction
<b>Pd</b>	Palladium
<b>Pd/H<sub>2</sub></b>	Palladium Hydrogen Electrode
<b>PGM</b>	Platinum Group Metal

<b>RE</b>	Reference Electrode
<b>SC</b>	Single Crystal
<b>SHE</b>	Standard Hydrogen Electrode
<b>SERS</b>	Surface-Enhanced Raman Spectroscopy
<b>SPM</b>	Scanning Probe Microscopy
<b>SPR</b>	Surface Plasmon Resonance
<b>STM</b>	Scanning Tunneling Microscopy
<b>UPD</b>	Underpotential Deposition
<b>TERS</b>	Tip-Enhanced Raman Spectroscopy
<b>WC</b>	Tungsten Carbide
<b>WE</b>	Working Electrode
<b>XPS</b>	X-ray Photoelectron Spectroscopy

# Introduction

A lot of research has been done with the aim to increase the ability of noble-metal surfaces to catalyze chemical reactions.<sup>[1],[2],[3]</sup> Catalytic reactions vary from redox reactions, in which one of the reactants is reduced or oxidized on the metal electrode to chemical reactions in which two reactants form a new species on the metal catalyst surface.

Analogous to the variety of reactions that can be catalyzed by noble metals, there is also a great number of possible catalysts.<sup>[1]</sup> Bulk metals have been widely studied for their ability to catalyze various chemical reactions.<sup>[4],[5]</sup> Transition metals from the platinum group (PGMs) are of main interest for reactions like hydrogen evolution reaction (HER), oxygen reduction reaction (ORR) or oxygen evolution reaction (OER), that are all of research interest in the field of fuel cell development<sup>[6],[7]</sup>. Many PGM bulk metals like platinum, palladium or iridium are good catalysts for reactions like HER, ORR and OER. Bulk PGM electrodes, however, are very expensive materials.<sup>[3]</sup> The reduction of costs for catalysts to make fuel cells more cost efficient is therefore of interest. One key indicator is the mass activity of a catalytically active material. The mass activity is defined as the ratio of catalytic activity to the mass of active electrode material. An increase in mass activity would result in cheaper electrode materials and, therefore, would make fuel cells more cost efficient.

One way to increase mass activity of PGM electrodes is to design the electrodes surface in a way that maximizes the number of catalytically active sites. A tool which can help to give insight in the question where the active catalyst sites are situated is electrochemical tip-enhanced Raman spectroscopy (EC-TERS). With EC-TERS it is possible to obtain Raman spectra of a surface with spatial resolution, which makes it possible to study electrochemical reactions under potential control under *operando* conditions on the electrode's surface.<sup>[8]</sup> EC-TERS allows a spatial resolution of 3 nm in air and molecular resolution of less than 1 nm under UHV conditions.<sup>[9]</sup>

The aim of this work was the design of a bimetallic surface that shows catalytical activity for HER, ORR and formic acid oxidation and that can be studied with EC-TERS. Au(111) surfaces were modified with Pd and Ir islands and characterized. For preparation and characterization of the model surfaces, cyclic voltammetry (CV), scanning tunneling microscopy (STM) and x-ray photoelectron spectroscopy (XPS) have been used. The island dimensions and dispersion were varied to obtain information about the influence of Pd/Au(111) and Ir/Au(111) interfaces on the activity of the substrate for HER, ORR and formic acid oxidation. EC-TERS can be used to study catalyzed reactions on the model surface to characterize the active sites. This is useful to design catalyst materials specifically to contain a high number of active sites in order to increase the mass activity for the catalyst and decrease the costs of fuel cells in future.

# Theoretical Fundamentals

## 2.1 Noble-metal surfaces

The atoms of a metal single crystal are ordered in a three-dimensional periodic lattice. The smallest possible, by translation periodically repeated unit of such a lattice is called unit cell. That unit cell is composed of three vectors, the lattice vectors  $\vec{a}_x$ ,  $\vec{a}_y$  and  $\vec{a}_z$ . The length of the lattice-vectors corresponds to the respective lattice constants. Most

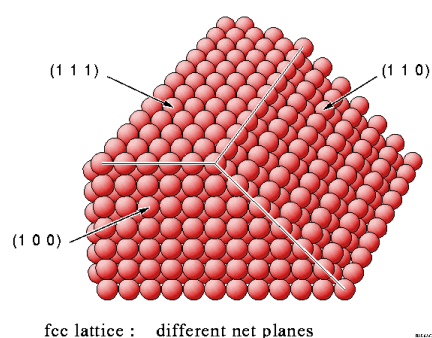


**Fig. 2.1:** Atom arrangement in the (100), (11) and (111) planes.

transition metals crystallize in the cubic crystal system<sup>[10]</sup> and form face-centered (fcc) or body-centered (bcc) cubic lattices. The metals that are treated in this work, gold, palladium and iridium, all crystallize in a fcc lattice. In the cases of these three metals, the fcc lattices correspond to the cubic closest packing (ccp) of the metal atoms. In the ccp, the atoms are arranged in three layers that are shifted against each other and that repeat periodically in the order ABC-ABC. A real single crystal does not have an infinite translational symmetry. Instead, the crystals have boundaries that are called crystal facets. Facets are indicated by Miller indices (hkl) that describe the arrangement of the surface atoms on the crystal boundaries. The different facets have different surface atom densities, depending on the Miller plane that describes the respective facet.<sup>[12]</sup> The largest possible surface atom density in the fcc lattice has the (111) plane in which the surface atoms are arranged in a hexagonal way.

Real crystals also have lattice defects in their bulk structure. Some of the most important

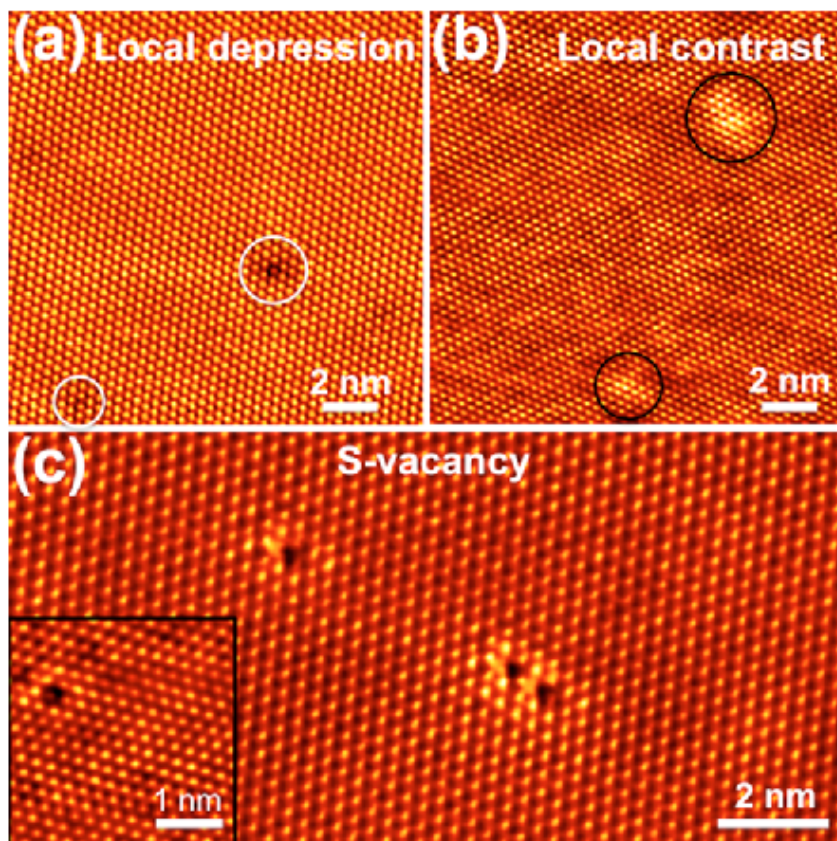


**Fig. 2.2:** Defects on atomic scale of an aMoS<sub>2</sub> surface. High resolution STM images of local depressions (a), local contrast (b) and S-vacancies (c) on the surface.<sup>[11]</sup>

of these defect structures are point defects and dislocations of atoms. Moreover, single crystal surfaces also contain defects, that are often the result of technical limits in the preparation of the single crystals.<sup>[13]</sup> Surface defects, for example, are step edges, adatoms, kinks and atom vacancies. Some of these defects are shown in figure 2.3. Studies have shown that defect sites of single crystal surfaces show higher reactivity than defect-free parts of a surface.<sup>[15–17]</sup> These studies can be used to design metal surfaces for the use as catalysts. The optimum amount of surface defects can be found to improve the catalytic activity of the surface.

The gold(111)-surfaces used in this work also showed the above-mentioned surface defects. Characteristic for well-grown Au(111) surfaces are the wide and atomically flat terraces in the size of several hundred nanometers that are separated by monoatomic high step edges.<sup>[18–20]</sup>

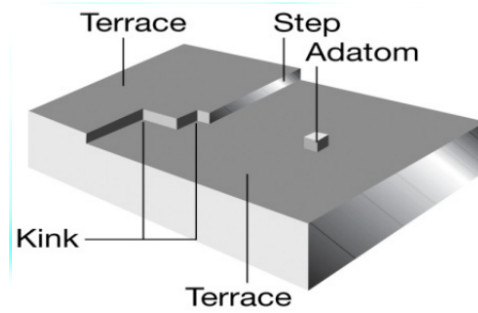


**Fig. 2.3:** Schematics of the surface defects of single crystals.<sup>[14]</sup>

## 2.2 Electrochemical metal deposition and metal displacement

Reactions that are associated with an electric current flow can be forced or controlled by applying an external voltage through a potentiostat. The subprocesses of a redox reaction, oxidation and reduction, run separated in space at different electrode surfaces. The classical 3-electrode setup is shown in figure 2.4. The potential applied to the

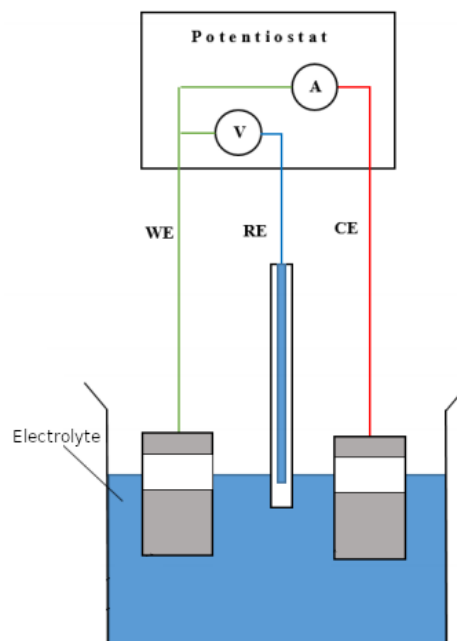


**Fig. 2.4:** Schematics of an electrochemical cell using a three-electrode setup.<sup>[21]</sup>

working electrode (WE) is controlled by a bipotentiostat with respect to an electrode of

defined potential, called the reference electrode (RE). It is possible to apply a very well-defined voltage between the electrodes, allowing precisely control of electrochemical processes at the WE. The current flowing between working- and counter-electrode during the reaction is measured and provides information about the ongoing reaction when plotted against the applied voltage. If the potential is ramped up and down linearly in time as done in cyclic voltammetry, the resulting plot is called a cyclic voltammogram (CV).

Platinum group metals (PGMs) like palladium or iridium are known to be good catalysts for various chemical and electrochemical reactions<sup>[1, 2]</sup>. It is possible to deposit them onto other metals from their respective salts. For the electro-deposition, a metal salt is added to an electrolyte solution. The salt is reduced at a certain applied voltage at the WE and the elemental metal is deposited (figure 2.5). The layer thickness formed

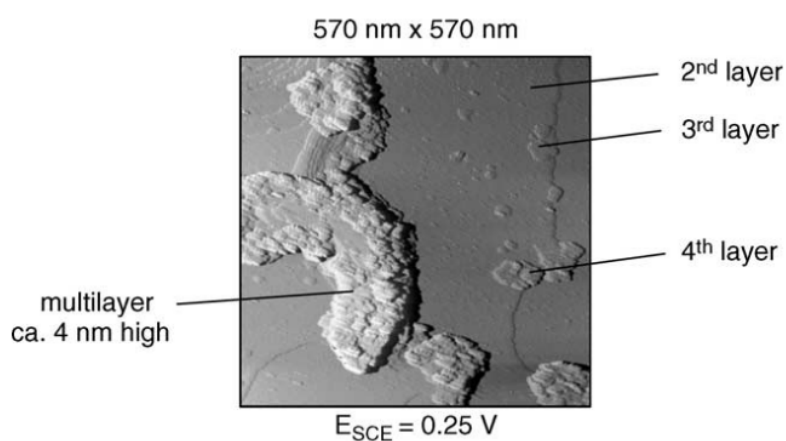
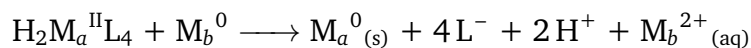


**Fig. 2.5:** STM image (570 nm × 570 nm) of Au(111) partially covered with Pd, obtained at 0.25 V in 0.1 M H<sub>2</sub>SO<sub>4</sub>, after deposition of four monolayer equivalents of Pd at 0.4 V.<sup>[22]</sup>

on the electrode's surface by direct metal deposition can vary from a submonolayer up to multilayer.<sup>[23]</sup> Another versatile tool for depositing thin PGM layers on an electrode up to less than a monolayer in thickness is metal displacement.<sup>[24]</sup> In this process, an ignoble metal is deposited and is replaced in a subsequent step by a more noble metal in sense of a redox reaction. Often the ignoble metal is copper, which can be easily deposited on a substrate by underpotential deposition (UPD).<sup>[25]</sup> Special about a CuUPD is that the deposition of copper from its salt already starts at a potential less negative than the Nernst potential (equilibrium potential). The equilibrium potential in this case means the potential at which copper starts to deposit onto itself. Copper adsorbs more easily on gold than on itself, making it energetically less favourable to deposit more

copper as soon as there is one third of a monolayer of copper on the gold surface.<sup>[25]</sup> CuUPD is a highly controllable process. The resulting copper layers can be tuned in terms of surface coverage and thickness.

For the subsequent displacement step, the more noble metal is used in form of its salt. When the substrate with CuUPD layer is immersed into the salt solution, the redox reaction shown in scheme 2.6 will start spontaneously. The more noble metal gets



**Scheme 2.6:** Redox reaction that happens at the substrate surface during the displacement reaction.

reduced and occupies the lattice spaces of the ignoble metal, which is oxidized and dissolved. CuUPD displacement represents an elegant method to deposit PGMs. The

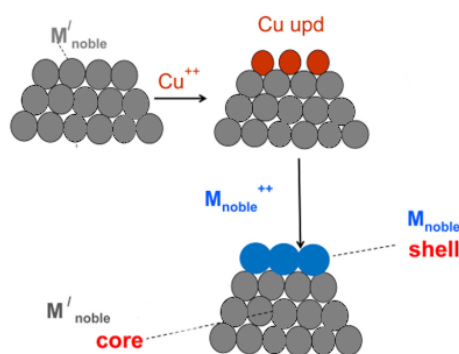


**Fig. 2.7:** Schematics of the electrochemical displacement of one metal by another more noble metal.<sup>[26]</sup>

advantage of CuUPD with subsequent metal displacement route over the direct PGM deposition is that it is more controllable to obtain 2D structures. Direct PGM deposition can lead to 2D or 3D structures, depending on the metal's behaviour in the deposition process.<sup>[22]</sup> Metals that adsorb more easily onto themselves than onto the substrate are more likely to grow 3D structures while metals like copper that adsorb more easily onto the substrate than onto themselves are more likely to grow 2D structures.<sup>[22]</sup>

## 2.3 Electrocatalysis

The choice of suitable electrode materials is crucial for many technically important electrochemical reactions, for example, in fuel cells. Fuel cells are the research objective of

many current studies in the field of "clean" and sustainable energy conversion. In a fuel cell, for example, alcohols or hydrogen can be converted to clean products. The selection of the electrode catalyst material has great influence on the efficiency of the reactions in a fuel cell. Ideally reactions should be run at the lowest possible overpotential, providing high activity and a long lifetime of the electrode at the same time. The better a certain electrode material catalyzes a reaction, the lower the overpotential that is necessary to run the reaction.<sup>[27]</sup>

One reaction of scientific interest to improve fuel cell efficiency is the oxygen reduction reaction (ORR). The ORR is kinetically inhibited, which results in a large overpotential and cell efficiency that is lower than theoretical calculations based on thermodynamics.<sup>[27]</sup> The ability of various metals to catalyze the ORR and reduce the overpotential has been studied for many years.<sup>[28]</sup> Figure 2.8 shows the activity of the bulk materials in a volcano plot. Following the Sabatier principle that states that the catalyst-substrate

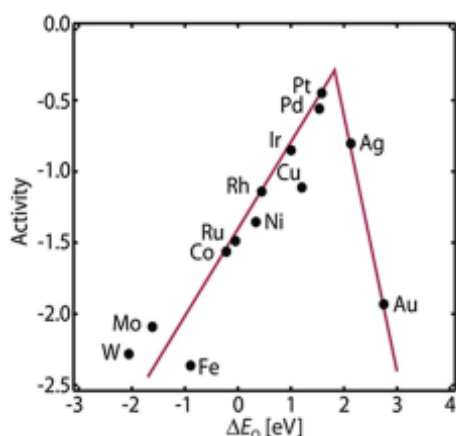


**Fig. 2.8:** Activity of different bulk metals to catalyze the ORR.<sup>[29]</sup>

interactions should not be too strong and also not too weak for the catalyst to be suitable for a given chemical reaction, the plot shows that platinum is the best bulk metal for the catalysis of the ORR, directly followed by palladium and iridium<sup>[29], [30]</sup>, the two metals that are used in this work. Also the oxidation of small organic acids like formic acid is relevant for the development of low-temperature fuel cells.<sup>[29]</sup>

The electrolysis of water requires catalyst materials to be highly active for the oxygen evolution reaction (OER) as well as for the hydrogen evolution reaction (HER). A lot of research has been done on both during the last years<sup>[1]</sup> as the reactions are of great industrial relevance.

Since PGMs are very expensive catalyst materials, the mass activity, i.e. the achievable power per mass of catalyst, is an important criterium in fuel-cell development. CHEN ET

AL.<sup>[5]</sup> demonstrated that Pt monolayers on a tungsten carbide (WC) substrate had the same catalytic activity for HER catalysis as a bulk-Pt-electrode, having material costs that are lower compared to bulk Pt by one order of magnitude. In this thesis, submonolayers of the PGMs palladium and iridium are tested as catalysts for the HER, ORR and formic acid oxidation. The main advantage of using PGMs as submonolayers over the use as bulk material is the use of less PGM material. The price and availability of the rare earth metals of the platinum group make it more favourable to use the least possible amount of PGM while maintaining activity for the catalysis of the reactions named before.

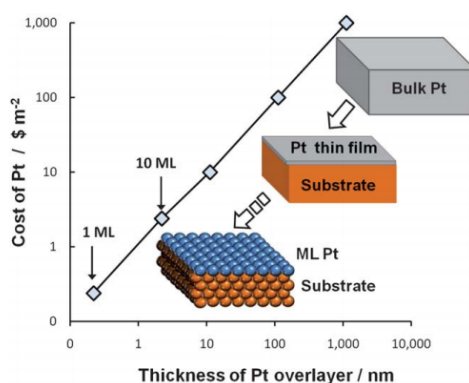


**Fig. 2.9:** Relation between thickness of a Pt-layer and the resulting material costs.<sup>[5]</sup>

Compared to platinum, iridium is more corrosion resistant and has a wide range of possible oxidation states. Bulk iridium oxide is also known as one of the best catalysts for the oxygen evolution reaction (OER) and due to its high stability it has become the industrial standard catalyst for that type of reaction.<sup>[6]</sup>

Palladium is also a suited catalyst for reactions such as ORR, HER and OER. It has been suggested for substituting platinum metal catalysts because of its similar properties and low price compared to platinum. Furthermore palladium showed higher resistance against CO poisoning than platinum electrodes.<sup>[7]</sup>

## 2.4 EC-TERS

Surface structures have great impact on the activity of catalyst materials.<sup>[31, 32]</sup> To study metal surfaces, there are a number of tools that all have their respective limitations. The resolution limit of optical microscopes is at the Abbe-limit, so that it is not possible to resolve objects smaller than 200-400 nm using conventional optical microscopy techniques

based on visible light.<sup>[33]</sup> The development of electron microscopes overcame that resolution limit because of the smaller wavelength of electrons compared to light. Electron microscopes have a spatial resolution of about 1 nm<sup>[34]</sup> while modern ones can also reach atomic resolution. A group of methods not based on matter-light interaction are scanning probe microscopes. SPM unites methods like scanning tunneling microscopy (STM) or atomic force microscopy (AFM). In STM, image contrast is achieved by having a strong distance dependency of a tunnelling current between the STM tip and the conductive sample. For this, a very sharp metal tip approaches the sample surface closely and a bias voltage is applied between tip and sample, resulting in a tunneling current that is measurable. If the tip is scanned over the sample surface, having a control circuit that either holds the distance or the resulting current constant, it results in a height profile image of the surface. With STM, it is possible to achieve atomic resolution.<sup>[35]</sup> All mentioned methods do not allow one to gain any information about the chemical composition or structure of a sample. IR and Raman spectroscopies, however, provide chemical information. Conventional Raman and IR spectra are bulk spectra, meaning that they provide information about the whole illuminated sample volume. The spatial resolution that can be reached depends on the experimental setup. I.e. focusing the incident laser light with an optical microscope can lead to a spatial resolution of micrometers.<sup>[36]</sup>

A combination of STM and Raman spectroscopy is tip-enhanced Raman spectroscopy (TERS). It was first postulated in 1984 by WESSEL<sup>[37]</sup> and experimentally realised by ZENOBI and coworkers in the year 2000.<sup>[38]</sup> In 1974, FLEISCHMANN ET AL. reported on the uncommonly high Raman-intensity of Pyridin molecules adsorbed on a Au-surface.<sup>[39]</sup> Later, the SERS effect (surface-enhanced Raman-spectroscopy) was explained by VAN DUYN and SCHATZ<sup>[40]</sup> based on the resonance of local surface plasmons that can enhance an incident electric field by a factor 10 or more which leads to an increase of Raman intensity by 6-12 orders of magnitude.<sup>[40]</sup> Based on the knowledge about the SERS effect, STM tips can be designed to strengthen the electric field in the previously mentioned way when they are illuminated by a laser source, increasing the resulting Raman signal of the molecules located under the apex of the tip in the tip-sample gap. The possibility to scan the tip across the surface allows one to collect information about the chemical structure and composition having a system dependent spatial resolution that is about 3 nm in air and less than 1 nm under ultra-high vacuum conditions.<sup>[9]</sup> It is possible to map a sample surface over a larger area to achieve topographical as well as chemical information of the sample at the same time with quasi-molecular spatial resolution.

EC-TERS allows one to investigate a sample in an electrochemical cell with potential

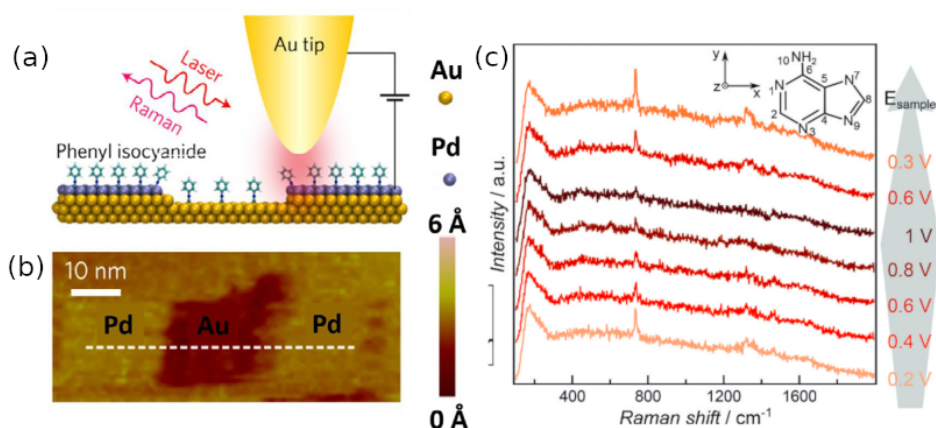


**Fig. 2.10:** (a): Schematics of the TERS principle with a gold tip that gets illuminated by a laser source being close to the sample surface.<sup>[41]</sup> (b): EC-STM image of a Pd/Au-surface.<sup>[41]</sup> (c): Potential-dependent Raman-spectras recorded using EC-TERS.<sup>[42]</sup>

control so that studies can be done under controlled reaction conditions.<sup>[8]</sup> EC-TERS studies on gold surfaces have shown that an oxidation at a given potential starts first at defect structures.<sup>[43]</sup>

BIN REN and coworkers were able to demonstrate site-specific electronic and catalytic properties of Pd/Au(111) bimetals using TERS<sup>[44]</sup>. They used phenyl isocyanate as probing molecule and observed the strength of the N-C-triple bond to show the difference in catalytic activity between Pd step-edges and Pd terraces. From DFT calculations they were able to show a higher d-band electronic profile for low-coordinated Pd on step-edges in comparison with higher coordinated Pd on terrace sites.

With the help of EC-TERS, it should be possible to observe surfaces of catalytically active materials under *operando* conditions to localize the active sites of the catalyst and classify reactions pathways.

# Results and Discussion

## 3.1 Choice of a suitable gold substrate

For evaluation of the quality and single-crystallinity of the substrates chosen to probe, cyclic voltammograms and STM-images were recorded of different kinds of substrates. The crystallinity of the used gold substrates was investigated by cyclic voltammetry. The samples were connected as working electrode to a bipotentiostat (Autolab PGSTAT 30) in a three-electrode configuration. The respective cyclic voltammograms were recorded in a range of 0.3 to 1.7 V vs. Pd/H<sub>2</sub> to see the predicted signals for order-/disorder-transition of the sulphate ions on the surface (1.1 V vs. RHE) and defect-/terrace oxidation at 1.4 V vs RHE and 1.6 V vs. RHE respectively. The evaluation of the crystallinity was done based on three characteristic signals of Au(111) in sulphate containing electrolyte, which are the order-/disorder-transition of sulphate ions adsorbed to the Au(111)-surface at 1.1 V vs. Pd/H<sub>2</sub> and based on the ratio of the area under the peaks of terrace oxidation at 1.6 V vs. Pd/H<sub>2</sub> to the oxidation of defects at 1.4 V vs. Pd/H<sub>2</sub>.

STM images of the substrate surfaces were recorded to visualize the surface structure. It was searched for wide and flat Au(111) terraces as required for the metal deposition experiments.

The substrates that were probed were gold-on-mica (150 nm gold on 150 μm mica, non-commercial, dimensions: cut to 12 mm x 12 mm), commercial gold-on-glass (Arandee, 0.7 mm borosilicate glass, 4 nm chromium, 250 nm gold layer, dimensions: 11 mm x 11 mm), non-commercial gold-on-glass (200 nm gold/10 nm chromim/glass, 13 mmx13 mm) that were made in house as well as bulk Au(111) single crystals (Mateck, 99.999%, Ø1 cm). The single crystals were used as internal standard for the evaluation of the quality of the other samples. Figure 3.1 shows an example cyclic voltammogram of a Au(111) single crystal compared to a non-commercial gold-on-glass substrate.

The single-crystal shows the strongest signal of the order-/disorder-transition (1.1 V vs. SHE) and the ratio of terrace oxidation peak (1.6 V vs. SHE) to defect oxidation peak (1.4 V vs. SHE) of 9.09. Moreover, the cyclic voltammogram shows the signal for sulphate adsorption at 0.52 V vs. SHE, which is typical for Au(111) electrodes in

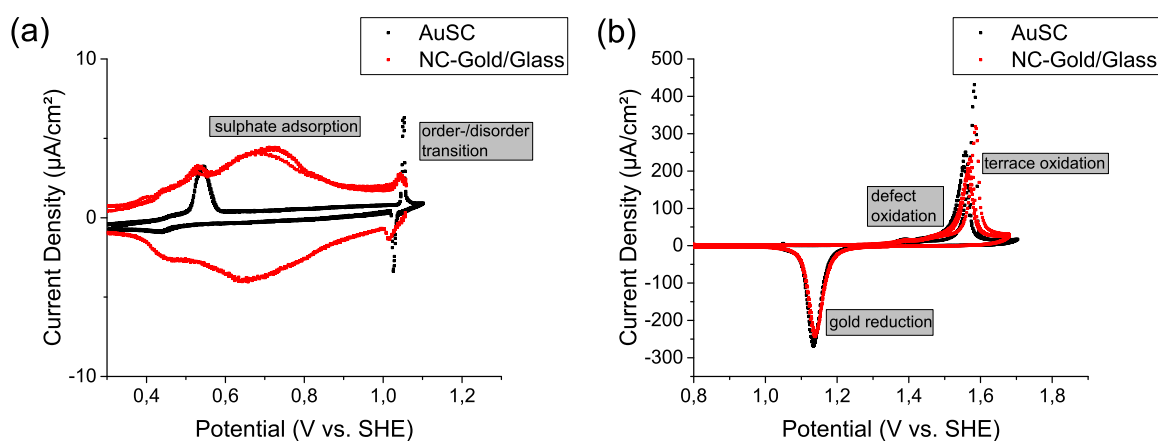


**Fig. 3.1:** Cyclic voltammograms of an Au(111) (black) in comparison to a non-commercial gold/glass sample (red). Recorded in 0.1 M  $\text{H}_2\text{SO}_4$  with a scan rate of 25 mV/s. (a): CV range 0.3 V to 1.1 V vs. SHE with signals for sulphate adsorption (broad signal) and order-/disorder-transition at 1.05 V vs. SHE. (b): CV range from 0.8 V to 1.7 V vs. SHE with signals for defect- and terrace oxidation (1.4 V and 1.6 V vs. SHE) and gold reduction (1.13 V vs. SHE).

**Tab. 3.1:** Integrated signals for order-/disorder-transition, defect- and terrace-oxidation of the tested samples normalized to the signal of the Au(111)-single-crystal and the respective terrace-to-defect-oxidation ratio.

	order-/disorder-transition	defect-oxidation	terrace-oxidation	terrace-to-defect-oxidation ratio
<b>Au(111) SC</b>	1	1	1	9.09
<b>comm. gold/glass</b>	0.41	0.86	0.35	3.69
<b>gold/mica</b>	3.35	/	/	/
<b>gold/glass</b>	0.30	1.60	1.04	5.91

sulphate containing electrolytes. Table 3.1 summarizes the respective integrated signals of order-/disorder-transition, defect- and terrace-oxidation for the tested gold substrates normalized to the respective current density of the Au(111)-single crystal. In addition, the terrace-to-defect-oxidation ratios are listed in the table.

The integration boundaries for defect- and terrace-oxidation were chosen to be 1.35 V - 1.5 V vs. SHE and 1.5 V - 1.7 V vs. SHE respectively. Integration was done after baseline correction using the second derivative for determination of the baseline. Cyclic voltammograms for the surface oxidation of the gold-on-mica samples could not be recorded because the gold adlayer peeled off the surface during the measurements, destroying the sample.

A well-suited substrate for the metal displacement experiments should have large terraces and a small amount of defects. An indication for this is the defect-to-terrace-oxidation ratio obtained from the CV. The best possible substrate obtained from analyzing the CV data was the Au(111) single crystal because its terrace-to-defect-oxidation ratio of 9.09 was the largest. The substrate was changed to the non-commercial gold-on-glass samples after three experiments with the single-crystal because it turned out that the method that was used to clean the crystal after an experiment was not sufficient for recovery of the clean, palladium-free gold surface which could be seen in the resulting CVs by a reduction of the order-/disorder-transition signal as well as in STM images. The non-commercial gold-on-glass substrates also showed a high terrace-to-defect-oxidation ratio of 5.91. The characteristic order-/disorder-transition signal was also observable in the CV which is why the non-commercial gold-on-glass samples were considered as substrates for later experiments. Furthermore, the STM-images showed wide and flat Au(111) terraces (fig. 3.2) similar to the ones of the Au(111) single crystal shown in figure 3.3.

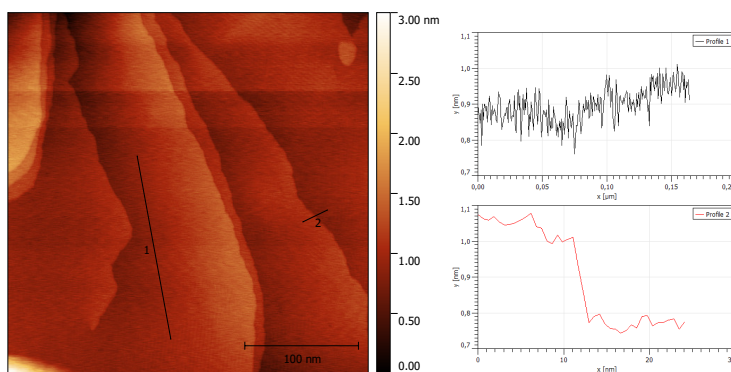


**Fig. 3.2:** STM image of the surface of a tested non-commercial gold-on-glass sample recorded with a Pt/Ir (80:20) tip at a scan speed of 1 line/s over a scan-range of 250 nm x 250 nm.

## 3.2 CuUPD

To determine the potential range for the CuUPD on the gold substrates, a cyclic voltammogram was recorded first in a copper-containing electrolyte (0.1 M H<sub>2</sub>SO<sub>4</sub>/1 mM CuSO<sub>4</sub>) over a wide potential window between 0.3 V and 0.85 V vs SHE with a Au(111) bead single crystal as working electrode (fig. 3.4). In agreement with literature, it shows two cathodic peaks of which the first one is the reduction of Cu<sup>2+</sup> to form one third

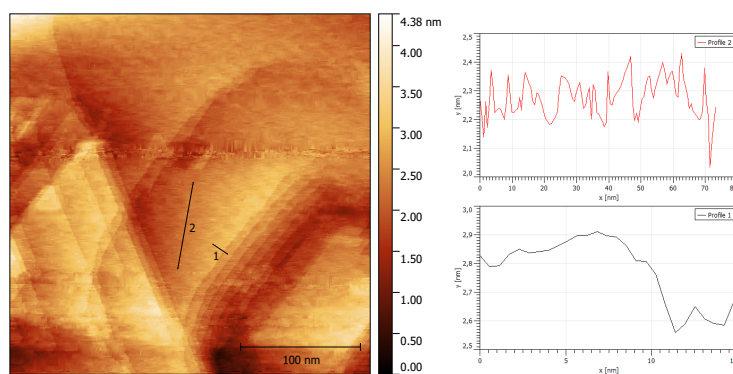


**Fig. 3.3:** STM image of the surface of a Au(111) single crystal recorded with a Pt/Ir (80:20) tip at a scan speed of 1 line/s over a scan range of 250 nm x 250 nm.

of a monolayer whereas the second peak at 0.35 V vs. SHE is the reduction of  $\text{Cu}^{2+}$  to complete one monolayer.<sup>[25]</sup> The signal at 0.35 V vs. SHE contains two peaks that are only separated on high quality Au(111) surfaces with a surface miscut of  $<0.5^\circ$ .<sup>[45]</sup> The two peaks correspond to the surface transition of Cu during the nucleation on steps (0.36 V vs. SHE) or terraces (0.34 V vs. SHE).<sup>[45]</sup> In the anodic scan direction, the peak at 0.4 V vs. SHE represents the oxidation of the first 2/3 of a monolayer. The shoulder is the counterpart of the separated reduction peaks, indicating the oxidation of Cu from steps. The second peak in anodic direction at 0.54 V vs SHE indicates the oxidation of the remaining 1/3 of the Cu monolayer.

For the deposition of a submonolayer of copper islands on the surface, a potential more negative than the first UPD peak at 0.53 V vs SHE and more positive than the second one at 0.35 V vs SHE was chosen for copper deposition. To investigate the influence of the potential on the size and distribution of the resulting islands, during the deposition, the experiments were performed at 0.44 V and 0.47 V vs SHE (red and green line in 3.4, respectively).

### 3.3 Systematic study of the influence of different deposition parameters on the size and distribution of the resulting Pd or Ir islands

Cu metal island's formation on gold was studied as a function of deposition time and deposition voltage. The samples were characterized before and after CuUPD and metal

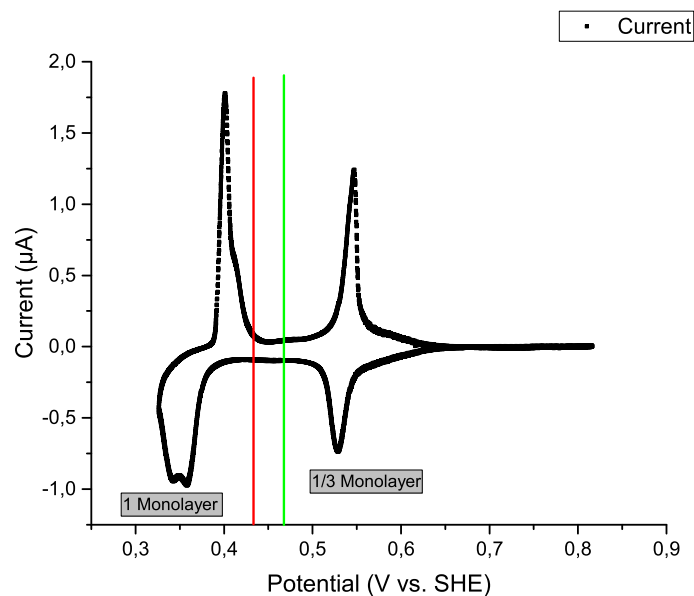


**Fig. 3.4:** Cyclic voltammogram recorded in 0.1 M  $\text{H}_2\text{SO}_4$ /1 mM  $\text{CuSO}_4$  at an immersion potential of 0.72 V vs. SHE with an Au(111) bead single crystal as WE, a gold wire CE and a copper wire RE. The red and green lines indicate the potentials chosen for UPD experiments.

displacement by cyclic voltammetry. STM images of the sample surface were recorded to study the size and distribution of the resulting Pd or Ir islands.

CuUPD deposition potentials were chosen to be at 0.44 V or 0.47 V vs SHE, respectively. 0.47 V vs SHE was chosen arbitrarily to be more negative than the peak for the formation of the first third monolayer. The second deposition potential of 0.44 V vs SHE was chosen to be more negative than the first one but still more positive than the second cathodic peak in the CuUPD CV. The duration of the CuUPD was varied between 2 s and 18 s.

The surface coverage was determined by integrating the current during copper deposition. The target metal deposition was confirmed by measuring the CV in the region of the HER and by comparing the respective CV to the CV of a Au(111) reference without CuUPD. The current-time trace of a copperUPD at 0.44 V is shown in figure 3.5.

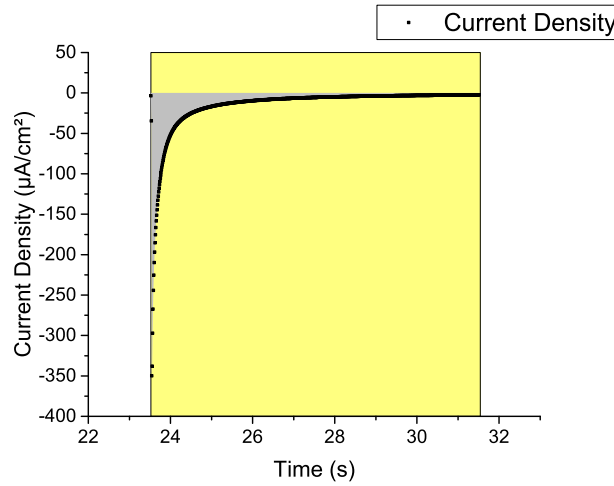


**Fig. 3.5:** Current density-time trace recorded during CuUPD on gold-on-glass. Parameters: 0.44 V vs SHE, 3 s deposition time. The immersion potential of 0.72 V vs SHE was held for 23.5 s before the CuUPD potential was applied. The integration area for surface coverage calculation is highlighted in gray.

The amount of charge needed for the deposition of a non-charged monolayer of copper on a Au(111) surface is  $Q_{ML} = 450 \mu\text{As}/\text{cm}^2$ .<sup>[46]</sup> The calculation of surface coverage from the current flowing during the CuUPD was made using the following equation (3.1) where  $Q_{UPD}$  is the transferred charge during CuUPD, and  $\Phi_{ML}$  is the resulting fraction of a copper monolayer that was deposited:

$$\phi_{ML} = \frac{Q_{UPD}}{Q_{ML}} = \frac{Q_{UPD}}{450 \mu\text{As}/\text{cm}^2} \quad (3.1)$$

The correlation between deposition time and surface coverage at different deposition potentials is shown in figure 3.6. The corresponding values are listed in table 3.2. Figure 3.6 shows that the surface coverage is strongly dependent on the deposition potential and deposition time. The dependence of the surface coverage on the deposition time is linear for short deposition times up to 6 s. The surface coverage increases slightly going from 0.24 ML at 3 s to 0.28 ML at 6 s with increasing deposition time. For longer deposition times >6 s, the slope of the increase in surface coverage flattens, reaching 0.30 ML at 10 s deposition time. For the more negative potential of 0.44 V vs SHE, the surface coverage at the same deposition time is larger than at 0.47 V vs SHE. The small difference in deposition potential of 0.03 V leads to a notable difference of about 0.04 up to 0.06 ML in surface coverage at same deposition time. For a deposition time of 3 s, the

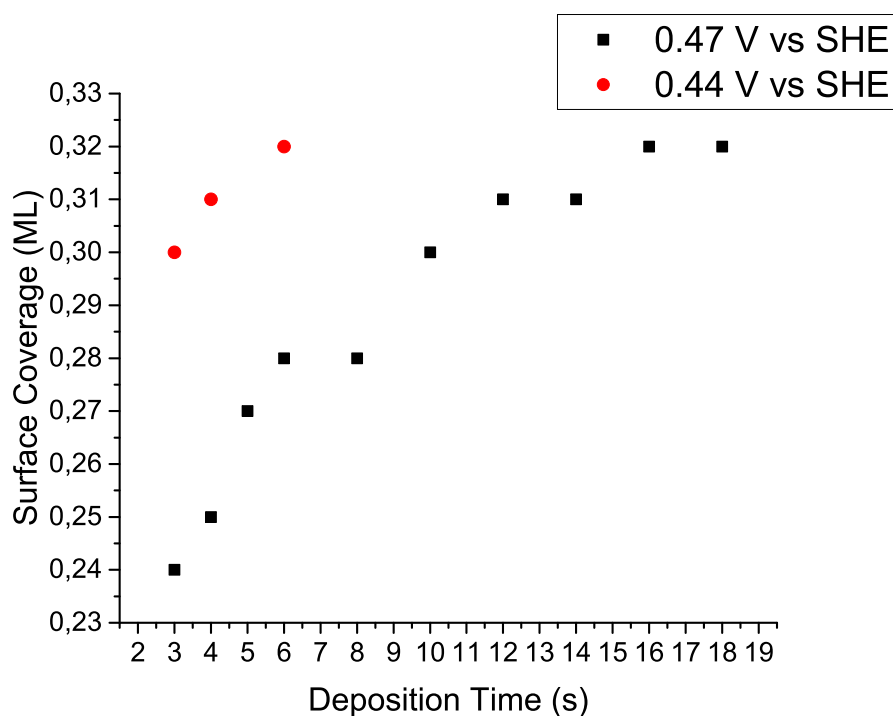


**Fig. 3.6:** Correlation between surface coverage as function of deposition time and deposition potential.

surface coverage is 0.24 ML for a deposition potential of 0.47 V vs SHE. For a deposition potential of 0.44 V vs SHE and 3 s deposition time, the surface coverage is 0.30 ML, an increase of 25%. The deposition potential has a greater influence on the resulting surface coverage than the deposition time. To reach a coverage of more than 0.30 ML with a deposition potential of 0.47 V vs SHE, a long deposition time of more than 10 s is needed, whereas 0.30 ML can be reached after 3 s using a deposition potential of 0.44 V vs SHE. The stronger potential dependency in comparison to the dependence on the deposition time is explainable by the exponential behaviour of the current vs time trace during the deposition. The initial current is strongly influenced by the potential but the current decreases strongly and is only about 25% of the initial current after a deposition time of 1 s. For a deposition potential of 0.44 V vs SHE, the initial current is 1100  $\mu\text{A}$ , for a deposition potential of 0.47 V vs SHE, the initial current is 492  $\mu\text{A}$ . The longer deposition time only has small influence on the surface coverage, the current vanishes with time during the deposition. For a deposition potential of 0.47 V vs SHE, the current after 1 s deposition time has decreased from 492  $\mu\text{A}$  to 6  $\mu\text{A}$ .

Figure 3.7 compares STM images of a clean Au(111) reference (3.7 a) and an Ir/Au(111) sample after copper deposition and displacement with iridium. Flat Au(111) terraces are

**Tab. 3.2:** Surface coverage calculated from current vs time traces measured at two deposition potentials and different deposition times.

Deposition Time [s]	Coverage 0.44 V vs. SHE [ML]	Coverage 0.47 V vs. SHE [ML]
3	0.3	0.24
4	0.31	0.25
5	/	0.27
6	0.32	0.28
8	/	0.28
10	/	0.30

seen in the clean reference (fig. 3.7 a). The image after CuUPD and iridium displacement (fig. 3.7 b) shows islands as bright spots on the surface. The height profile of the islands is shown in figure (fig. 3.7 d). The average island height is 0.37 nm which is close to the diameter of an iridium atom of 0.36 nm.<sup>[47]</sup> The average height of a Au step-edge is 0.30 nm (fig. 3.7 c), corresponding to a single-atom Au step-edge of 0.27 nm.<sup>[47]</sup>

STM images can be evaluated in terms of the existence of Ir-islands by comparing the images before and after CuUPD/Ir-displacement process. After the CuUPD and Ir-displacement, XPS experiments have been performed (s. appendix 6.24) that indicate the presence of Ir on the sample surface. The CV of the sample shows a clear difference between the CV of the clean Au(111) surface before the deposition/displacement process and after the process. The potential range that was studied was from -0.2 V vs SHE to 0.5 V vs SHE, to cover the range in which the HER takes place (0.06 V to <-0.2 V vs RHE). Gold is a weak catalyst for the HER which can be seen in the CV as a flat slope in the HER region. For metals that are better catalysts for the HER, like palladium and iridium, the slope is steeper and the onset for both metals is at more positive potentials than for Au(111). Comparing the slope and the onset of the HER peak in the CVs shows that the HER begins at more positive potentials (-0.06 and -0.10 V vs SHE for Pd/Au(111) and Ir/Au(111), respectively) and is stronger after the deposition/displacement process than before. This is an indication for the presence of Ir on the surface (figure 3.8). The presented experimental data allow the conclusion that the islands in the STM images are Ir islands.

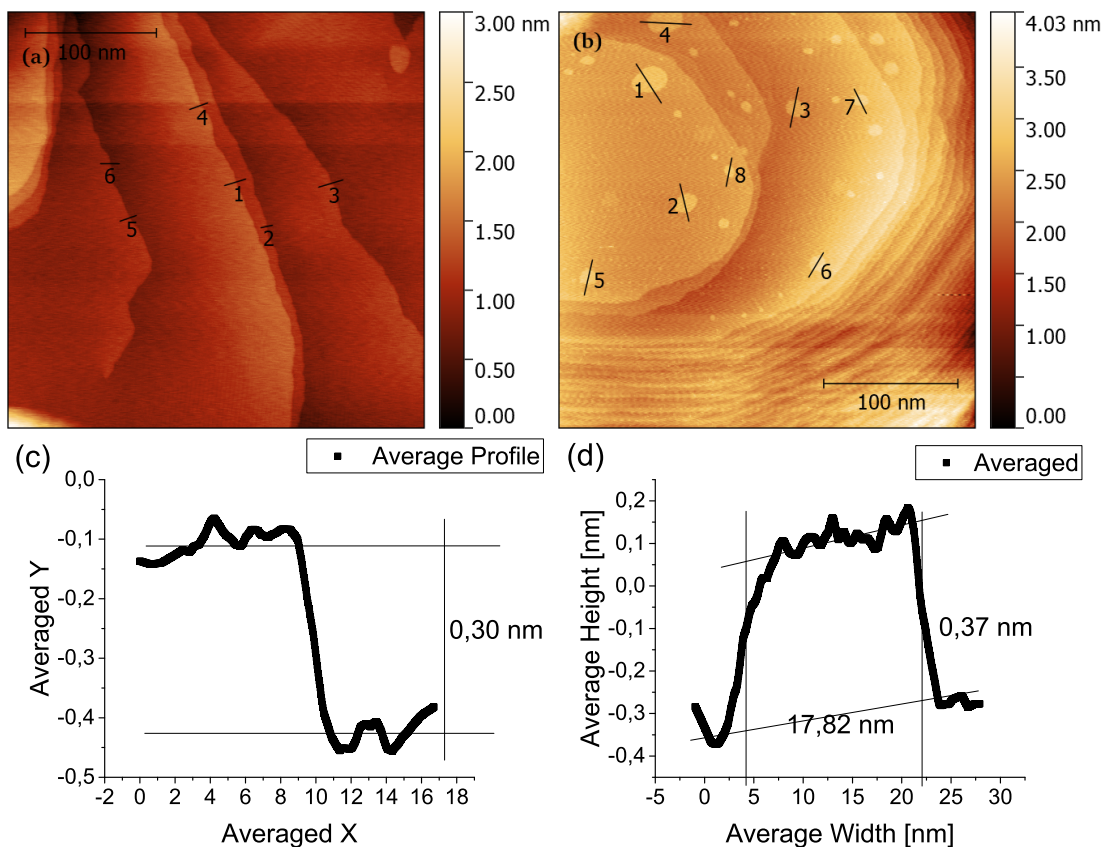


**Fig. 3.7:** STM images of a clean Au(111) sample (a) and of an Ir/Au(111) sample (b) and the average height profile of the Au step edge extracted from 5 individual height profiles of Au step edges (c) and the average height profile of Ir islands from individual height profiles of 10 islands (d).

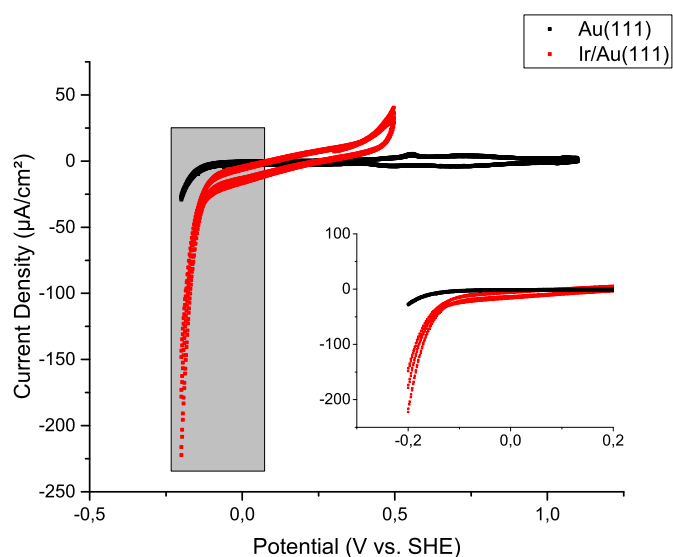


**Fig. 3.8:** Cyclic voltammogram of a clean Au(111) sample in comparison to the same sample after Ir was deposited on the sample surface. The inset shows the same CV cut at 0.2 V vs SHE to show the HER onset.

Similar experiments were performed for Pd/Au(111). A STM image and average height profile of Pd islands on Au(111) is shown in figure 3.9. As described before for Ir islands, the Pd islands appear as bright spots in the STM image. The average island height calculated from all samples is 0.28 nm which is in accordance to the diameter of a palladium atom (0.28 nm)<sup>[47]</sup>. The CV shows the presence of a metal that is active for HER catalysis (fig 3.10). The charge density under the HER peak is much higher after the CuUPD/Pd displacement procedure (green, 228.9  $\mu\text{As}/\text{cm}^2$ ) than for the pristine Au(111) surface (black, 4.3  $\mu\text{As}/\text{cm}^2$ ). The experimental results allow the conclusion that the islands in the STM image (fig 3.9) are Pd islands.

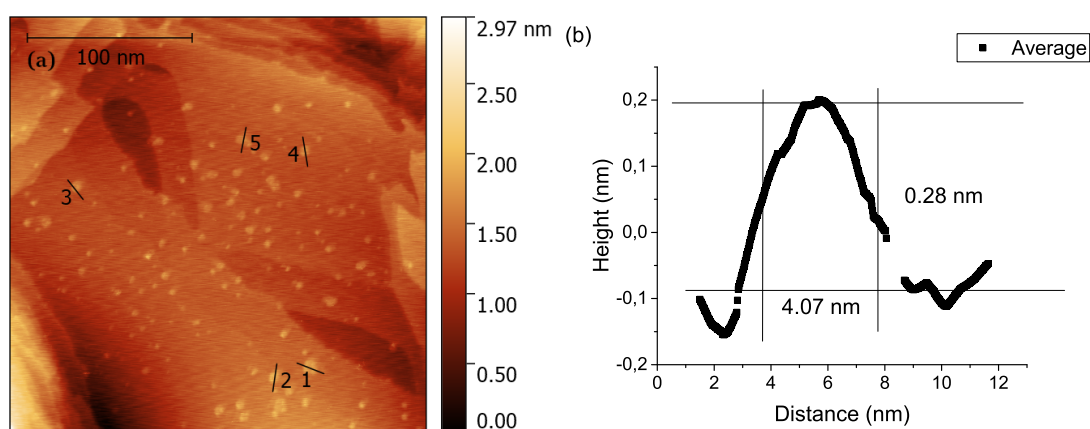


**Fig. 3.9:** (a) STM image of a Pd/Au(111) sample after CuUPD and Pd displacement procedure. (b) Average height profile of the Pd islands.

Figure 3.11 shows Pd/Au(111) after 6 s deposition time at a deposition potential of 0.47 V vs SHE (a) and a deposition potential of 0.44 V vs SHE (b). When the deposition was performed at 0.44 V vs SHE, the images shows islands of small size ( $3.4 \text{ nm} \pm 0.5 \text{ nm}$ ) and a high surface coverage (0.32 ML). The island size is uniform (standard deviation (STD): 0.5 nm) as well as the distribution of the islands on the surface. At a more positive deposition potential of 0.47 V vs SHE, the islands have an average size of  $13.8 \text{ nm} \pm 3.8 \text{ nm}$  which is 4 times larger than at a deposition potential of 0.44 V vs SHE. The overall surface coverage at 0.47 V vs SHE is 0.04 ML less than at 0.44 V vs SHE at 6 s deposition potential. The island size distribution is larger for a deposition potential of 0.47 V vs SHE (STD: 3.8 nm) than for a deposition potential of 0.44 V vs SHE (STD: 0.5 nm) and there are fewer islands than at a deposition potential of 0.44 V vs SHE.

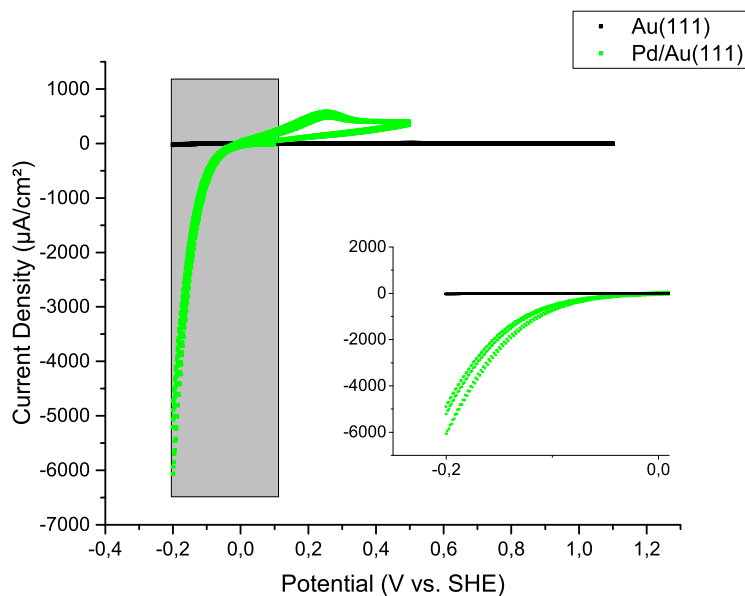


**Fig. 3.10:** Cyclic voltammogram of a clean Au(111) sample (black) in comparison to the same sample after CuUPD and Pd displacement procedure (green). The inset shows the region highlighted in grey.

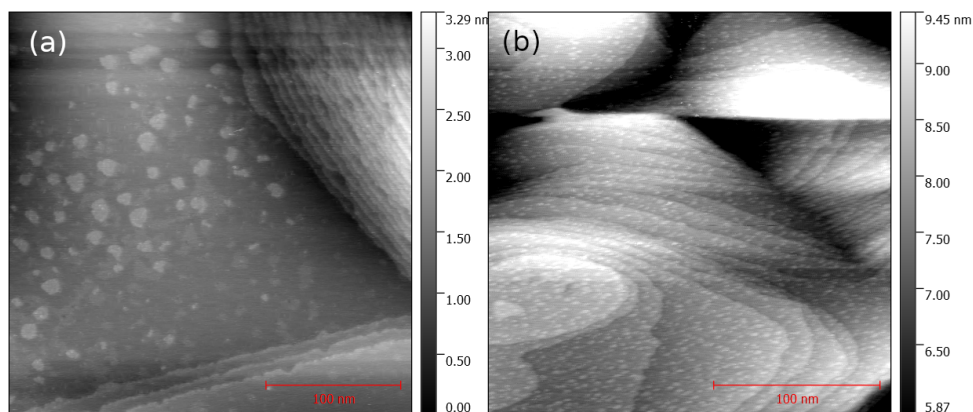


**Fig. 3.11:** STM images of Pd/Au(111). (a) Deposition potential 0.47 V vs. SHE (b) deposition potential 0.44 V vs. SHE, at 6 seconds deposition time.

Island sizes of the respective samples at different metal deposition parameters as determined from analyzing the STM images are summarized in tables 3.3 (Ir) and 3.4 (Pd) and the results are plotted in figure 3.12. The average Pd island size at a deposition potential of 0.44 V vs SHE increases with increasing deposition time, going from 2.3 nm

**Tab. 3.3:** Ir island sizes depending on different deposition potentials and deposition times.

deposition time [s]	Ir island size 0.44 V vs. SHE [nm]	Ir island size 0.47 V vs. SHE [nm]
3	/	10.1 nm ± 1.5 nm
5	/	11.2 nm ± 1.9 nm
6	/	17.8 nm ± 4.2 nm
9	/	30.8 nm ± 8.3 nm
12	/	12.9 nm ± 3.9 nm

**Tab. 3.4:** Pd island sizes depending on different deposition potentials and deposition times.

deposition time [s]	Pd island size 0.44 V vs. SHE [nm]	Pd island size 0.47 V vs. SHE [nm]
3	2.3 nm ± 0.6 nm	5.2 nm ± 0.7 nm
4	2.8 nm ± 0.6 nm	6.3 nm ± 1.6 nm
5	3.0 nm ± 0.4 nm	7.6 nm ± 1.3 nm
6	3.4 nm ± 0.5 nm	13.8 nm ± 3.8 nm
10	/	11.8 nm ± 2.6 nm

± 0.6 nm at 3 s to 3.4 nm ± 0.5 nm at 6 s. At a deposition potential of 0.47 V vs SHE, the average island size increases from 5.2 nm ± 0.7 nm at 3 s to 13.8 nm ± 3.8 nm at 6 s and drops to 11.8 nm ± 2.6 nm at 10 s. The slope of the increasing island size is greater for a deposition potential of 0.47 V vs SHE than for 0.44 V vs SHE.

The CuUPD current density-time trace (fig. 3.4) does not show a minimum-maximum peak as it would be expected for a deposition process following the nucleation and growth law.<sup>[48]</sup> Instead, the exponential decay of current density with time indicates a diffusion controlled process. The results of the STM analysis of islands grown at different deposition potentials show that the average island size is larger for depositions at more positive potentials. This indicates that the deposition potential plays a role in the nucleation process. The lower deposition potential allows more nuclei to form at the short time frame that is limited by diffusion, leading to a larger amount of islands on the surface than at more positive deposition potentials. In the following growth phase that it also diffusion limited, the current density decays equally for both deposition potentials. That means that the islands in both cases grow in the same manner, controlled by the diffusion of copper ions to the electrode. In case of more negative deposition potentials, where more islands were formed, the islands grow smaller on average compared to more positive deposition potentials, because the overall amount of copper that gets deposited

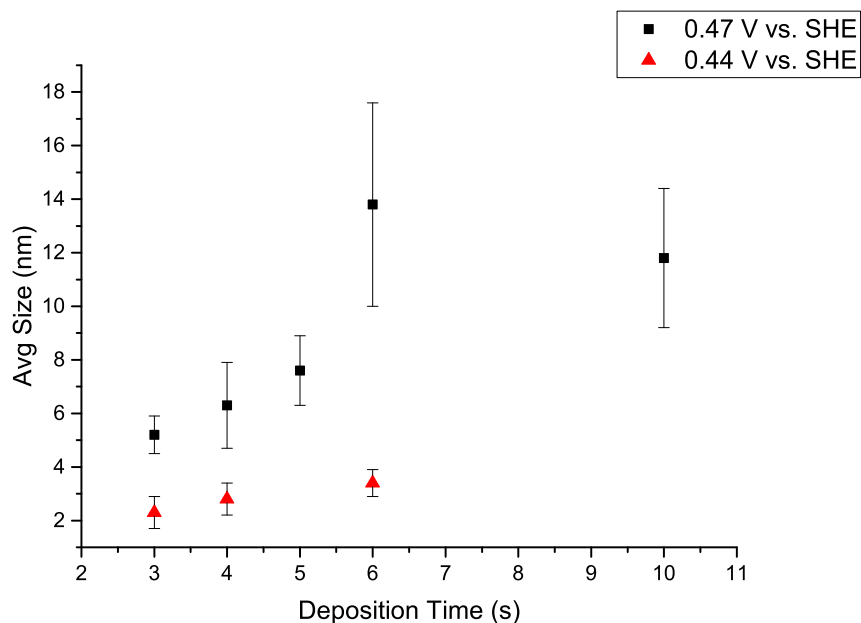
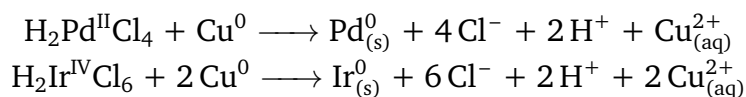


**Fig. 3.12:** Correlation between the size of the Pd islands and deposition time of copper on Au(111) at different deposition potentials.

after the initial nucleation is the same because of the diffusion limit.

The influence of deposition potential on surface coverage is also apparent from the current density-time traces. At more negative deposition potential, the initial current density is larger, the slope of the decay is identical to the one of more positive deposition potential. That means that, starting from higher current density decaying with the same slope, more copper is deposited at more negative potentials than at more positive deposition potentials. Because of the nucleation process described above, also the average distance between the islands is potential dependent. At a more negative deposition potential, more nuclei are formed which leads to a distance between the islands that is smaller on average compared to the distances resulting from a more positive deposition potential.

The data show that the iridium samples display many small islands (1-3 nm) on the surface and only few bigger islands (13 nm) (fig. 3.13). The possible explanation for the high number of very small islands can be given considering the displacement reactions of Cu versus Pd and Ir (scheme 3.1). Figure 3.13 shows a pictorial comparison between the Pd and Ir islands.



**Scheme 3.1:** Redox reactions for the Pd and Ir displacement reactions respectively.

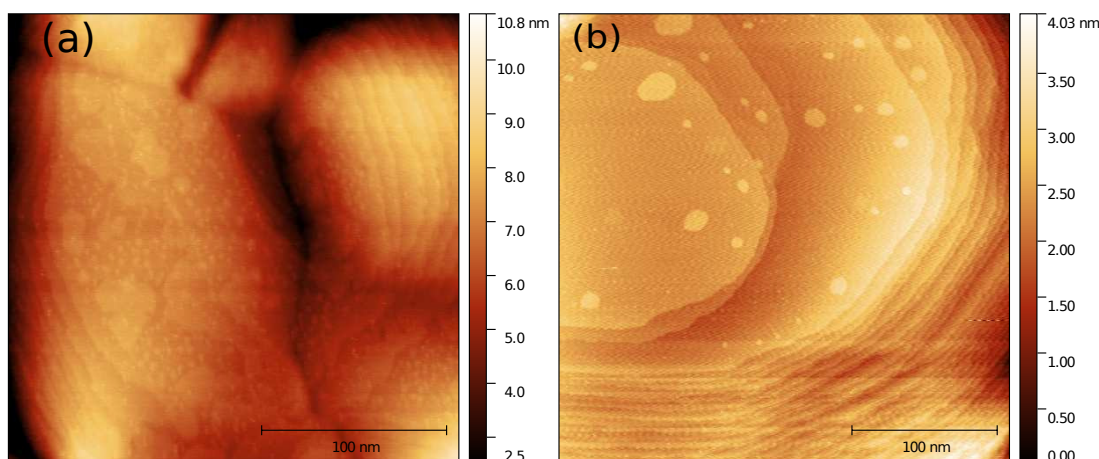


**Fig. 3.13:** STM images of gold surfaces with Pd (a) and Ir islands (b) CuUPD potential 0.47 V vs. SHE, 6 seconds deposition time.

For the Pd displacement, a bivalent Pd salt ( $\text{H}_2\text{PdCl}_4$ ) with an electron ratio to Cu of 1:1 when exchanged with  $\text{Cu}^{2+}$  is used. Ir is used in form of its hydrochloride ( $\text{H}_2\text{IrCl}_6$ ) with an Ir ion with a charge of +4. In accordance with the redox reaction, two copper atoms need to be oxidized to reduce one Ir ion to fulfill the electron balance. As a consequence, the Cu islands are ripped apart into smaller agglomerations of Ir atoms during the Ir displacement process. Also the diameter of one Pd or Ir atom plays a role in the size of the resulting islands. The diameter of one Iridium-atom is 0.36 nm<sup>[47]</sup>, the diameter of one Pd-atom is 0.28 nm.<sup>[47]</sup> The size difference of 0.08 nm between Ir and Pd atoms leads to the need of more Pd atoms to form an island than for an Ir island of the same size. Provided that the respective metal atoms form a hexagonal pattern on the Au(111) surface, 88 Pd atoms can form an island of 3 nm size. For comparison, 55 Ir atoms are needed to form an island of the same size. Only 62.5% of the amount of Pd atoms are needed to form Ir islands of the same size. As consequence of that, the resulting Pd islands are in average 38% of the size of Ir islands at the same deposition time.

### 3.4 Electrochemical stability of the islands

The long-term stability of the metal islands on gold were tested with CV in a potential range between -0.2 V to 0.5 V vs SHE in 50 cycles. The current density in the area of HER was used as an indicator for the presence of Pd or Ir on the Au(111) surface. HER on gold occurs at -0.13 V vs RHE whereas both Pd and Ir are better catalysts for the HER which starts at -0.06 V and -0.10 V vs SHE respectively. Also, the charge for the HER peak from the onset to -0.2 V vs SHE is higher for Pd and Ir than for gold (section 3.5). The HER current density is dependent on the amount of catalytically active Pd or Ir sites, so that a decrease of HER current density is an indicator of decreasing amount of Pd and Ir, respectively. A sample that is stable under the tested conditions will not show a reduction of HER charge during the experiment because the number of active Pd or Ir sites would not decrease. The CV of palladium is shown in figure 3.14. It shows that the

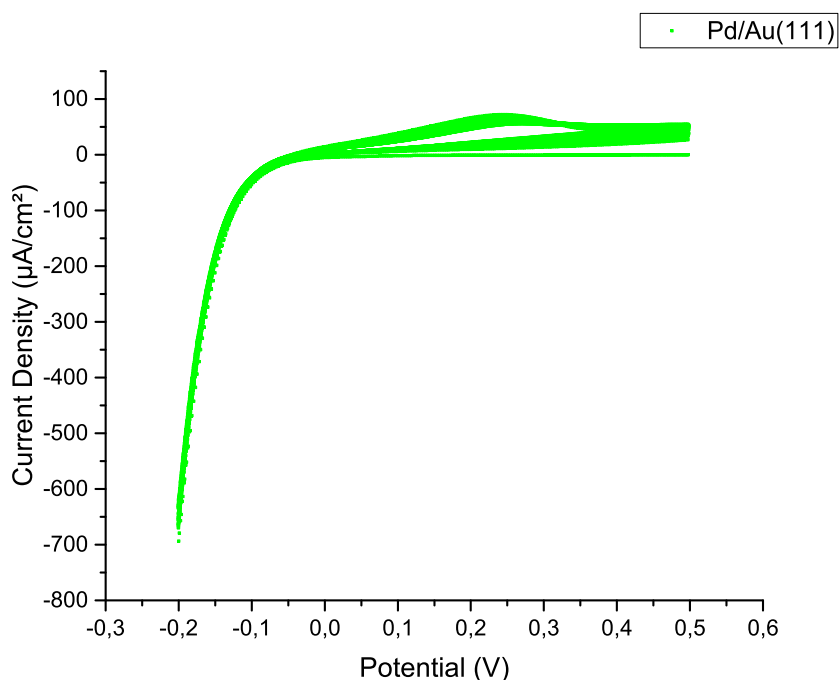


**Fig. 3.14:** Cyclic voltammogram of a Pd/Au(111) sample in the range of -0.2 V to 0.5 V vs SHE over 50 cycles at 25 mV/s scan rate with an immersion potential of 0.3 V vs SHE.

tested Pd islands are stable in the potential window for at least 50 cycles. The catalytic activity of the sample for the HER was constant over time. The same result is shown for Ir/Au(111) in figure 3.15. The islands are stable under electrochemical conditions for at

least 50 cycles from -0.2 V to 0.5 V vs SHE.

In addition to the long term stability test in a narrow potential range under electro-

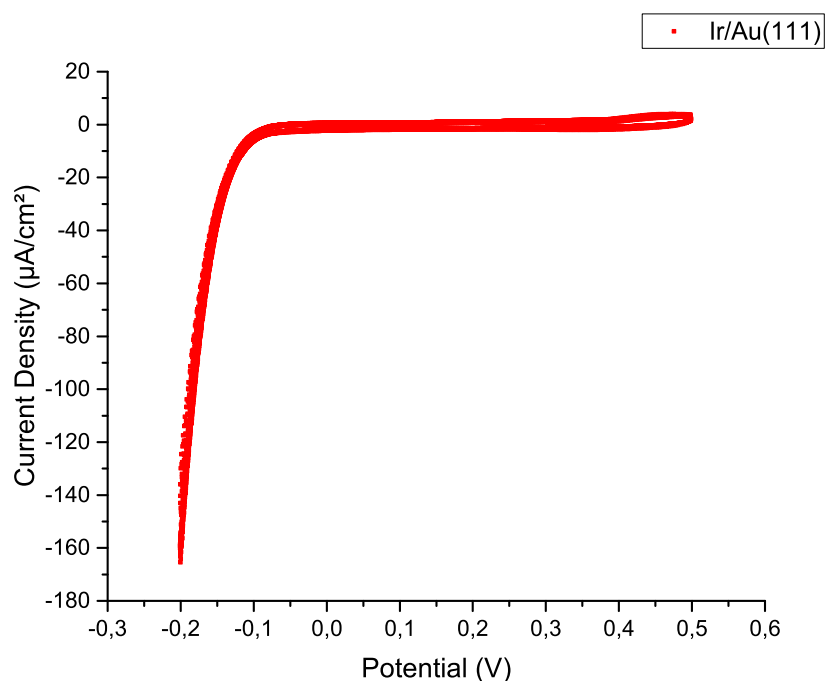


**Fig. 3.15:** Cyclic voltammogram of a Ir/Au(111) sample in the range of -0.2 V to 0.5 V vs SHE over 50 cycles at 25 mV/s scan rate with an immersion potential of 0.3 V vs SHE.

chemical conditions, the stability of the samples in a wider potential window was tested to obtain the maximum potential range that can be used for catalytic reactions under electrochemical conditions. For this, cyclic voltammograms were recorded with increasing potential range with upper potential varied between 600 mV and 1 V vs SHE until the degradation of the sample was visible in the CV by decreasing HER charge. Figure 3.16 shows that the tested samples were stable up to approximately 0.75 V vs SHE before the HER charge started to decrease and sample degradation occurred.

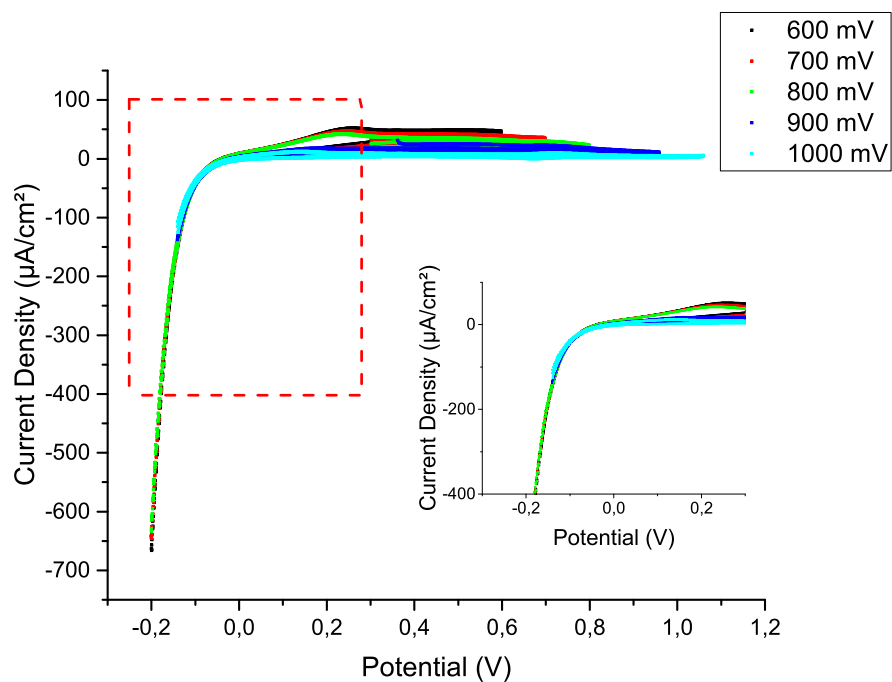


**Fig. 3.16:** Cyclic voltammogram of a Pd/Au(111) sample with different upper limit, starting with an upper limit of 0.6 V vs SHE up to an upper limit of 1 V vs SHE.

The distribution and size of the metal islands on the surface influence the island stability. Since the oxidation of defect sites is thermodynamically more favourable than the oxidation of terrace structures, island oxidation occurs first at the gold-surface/island interface. If the surface coverage is determined by a high amount of small islands, there are more gold/island interfaces and the oxidation starts at more negative potentials than on surfaces covered by bigger islands with the same surface coverage because more gold/island interfaces are available for oxidation.<sup>[49]</sup>

## 3.5 Hydrogen Evolution Reaction (HER)

All prepared samples were tested for their ability to catalyze the HER by performing cyclic voltammetry. Crucial parameters to judge the samples are the transferred charge during the HER and the onset potential of the HER. A pristine Au(111) sample was used as reference. The samples were cycled in a potential range between -0.2 V and 0.5 V vs SHE.

The onset potentials were determined by recording a CV on static 2D electrodes at scan rates of 25 mV/s. The values for the HER charge cannot be directly compared to values in literature. Here, we compare the onset potentials of HER of the samples that were tested using the same experimental conditions. The onset potential for clean gold was determined to be -0.13 V vs SHE (lit.: -0.02 V vs SHE (2 mV/s scan rate, 0.5 M H<sub>2</sub>SO<sub>4</sub>)<sup>[50]</sup>). The charge density was obtained by integration in the range from -0.13 V to -0.2 V vs SHE to be 1.67  $\mu\text{As}/\text{cm}^2$  for Au(111).

Figure 3.17 shows CVs of clean Au(111), Pd/Au(111) and Ir/Au(111) in the HER area from -0.2 V vs SHE to the respective HER onset up to 0.5 V vs SHE prepared by using the same deposition time for comparison. The onset potentials for Pd/Au(111) and Ir/Au(111) are -0.06 V and -0.10 V vs SHE respectively. The onset potential of Pd/Au(111) is +70 mV shifted against Au(111) and +40 mV shifted against Ir/Au(111). This is in qualitative accordance with the trend of the bulk materials that can be found in literature<sup>[1]</sup>. The HER charge was calculated to be 36.8  $\mu\text{As}/\text{cm}^2$  for Pd/Au(111) and 14.7  $\mu\text{As}/\text{cm}^2$  for Ir/Au(111) for deposition times of 12 s (surface coverage: 0.32 ML). The HER charge for Au(111) and Ir/Au(111) normalized to Pd/Au(111) is 0.05 and 0.4 respectively. Figure 3.18 shows the direct comparison between Ir/Au(111) and Pd/Au(111). The results show that Pd/Au(111) is a better catalyst for HER than Ir/Au(111). It has a more positive onset potential (+40 mV) and a higher HER charge.

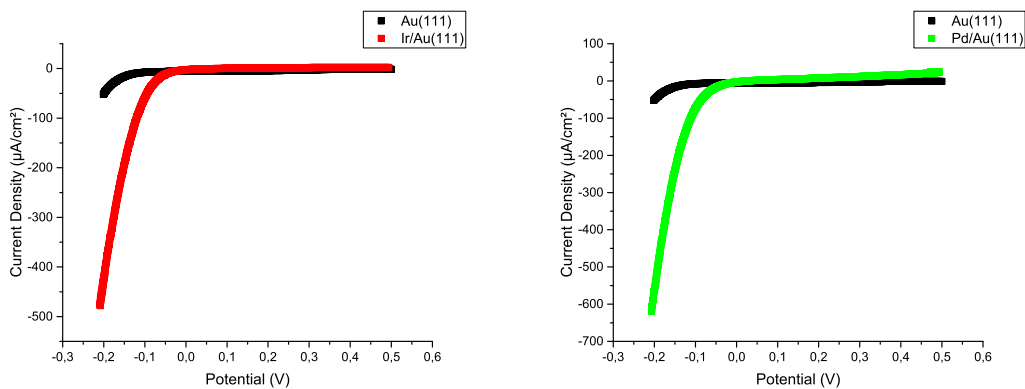


**Fig. 3.17:** Cyclic voltammogram of a clean Au(111) sample in comparison Ir/Au(111) (a) and Pd/Au(111) (b) in the range of -0.2 V to 0.5 V vs SHE. Immersion potential: 0.3 V vs SHE, scan rate 25 mV/s in 0.1 M  $\text{H}_2\text{SO}_4$ .

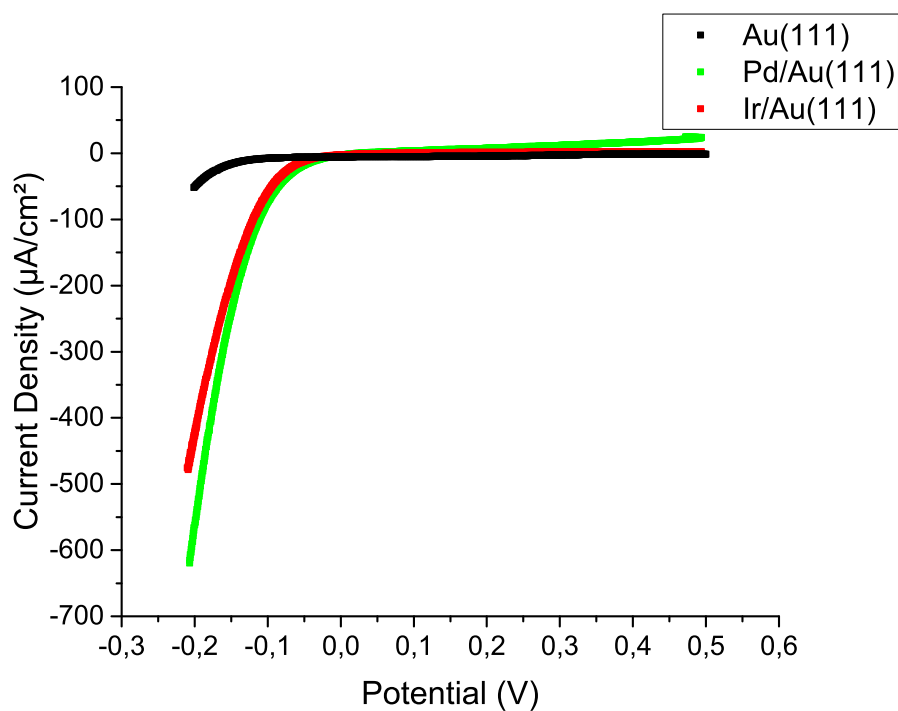


**Fig. 3.18:** Cyclic voltammograms of Pd/Au(111) (green) and Ir/Au(111) (red) compared to Au(111) (black) in the range of -0.2 V to 0.5 V vs SHE. Immersion potential: 0.3 V vs SHE, scan rate 25 mV/s in 0.1 M  $\text{H}_2\text{SO}_4$ .

**Tab. 3.5:** HER charge for different Pd/Au(111) samples in dependence of deposition time, island size and surface coverage.

deposition time [s]	Pd island size [nm]	surface coverage [ML]	HER onset [V]	HER Charge [ $\mu\text{As}/\text{cm}^2$ ]
3 (0.44 V vs. SHE)	2.3	0.30	/	114.2
4 (0.44 V vs. SHE)	2.8	0.31	/	78.5
5 (0.44 V vs. SHE)	/	0.31	/	155.7
6 (0.44 V vs. SHE)	3.4	0.32	/	196.8
3 (0.47 V vs. SHE)	5.2	0.24	/	/
4 (0.47 V vs. SHE)	6.3	0.25	-0.08	30.2
5 (0.47 V vs. SHE)	7.6	0.27	/	/
6 (0.47 V vs. SHE)	13.8	0.28	-0.06	30.8
10 (0.47 V vs. SHE)	11.8	0.30	-0.09	11.9
12 (0.47 V vs. SHE)	/	0.31	-0.08	47.8
14 (0.47 V vs. SHE)	/	0.31	-0.06	41.6
16 (0.47 V vs. SHE)	/	0.32	-0.07	36.8
18 (0.47 V vs. SHE)	/	0.32	-0.08	31.7

Tables 3.5 and 3.6 summarize the calculated HER charges and onset potentials for different Pd/Au(111) and Ir/Au(111) samples respectively. Figure 3.19 shows the correlation for Pd/Au(111) and Ir/Au(111) between HER current density, deposition time and island size respectively. It can be seen that the HER charge increases for both Pd/Au(111) and Ir/Au(111) up to a deposition time of 12 s and 14 s, respectively. For longer deposition times, the HER charge starts to decrease. The values for the Pd/Au(111) sample with 10 s deposition time and Ir/Au(111) with 12 s deposition time lie outside the trend. The decrease in HER charge for longer deposition times can be a result of merging of the islands during long grow durations as it was reported also for PdUPD by KOLB and coworkers.<sup>[22]</sup> This would result in less Au/island interfaces which may have impact on the HER catalysis ability if the active sites are mainly the Au/island interfaces.

**Tab. 3.6:** HER charge for different Ir/Au(111) samples in dependence of deposition time, island size and surface coverage.

deposition time [s]	Pd island size [nm]	surface coverage [ML]	HER onset [V]	HER Charge [ $\mu\text{As}/\text{cm}^2$ ]
3 (0.47 V vs. SHE)	10.1	0.24	/	/
6 (0.47 V vs. SHE)	13.0	0.28	-0.115	6.31
8 (0.47 V vs. SHE)	/	0.28	-0.116	7.17
10 (0.47 V vs. SHE)	/	0.30	-0.101	16.6
12 (0.47 V vs. SHE)	12.9	0.31	-0.114	3.34
14 (0.47 V vs. SHE)	/	0.31	-0.096	27.3
16 (0.47 V vs. SHE)	/	0.32	-0.108	14.7

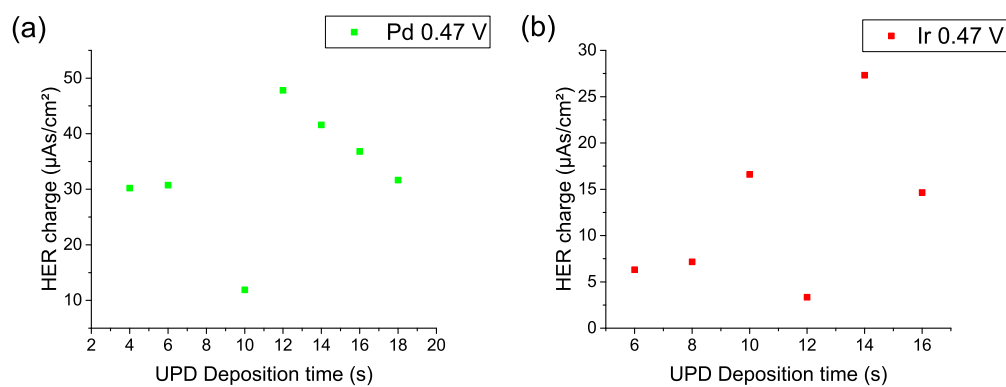


**Fig. 3.19:** Dependence of HER charge of Pd/Au(111) (a) and Ir/Au(111) (b) on deposition time.

## 3.6 Formic Acid Oxidation

Formic acid oxidation was performed with Pd/Au(111) samples of various deposition times. The resulting CVs did not show a peak for formic acid oxidation (fig. 3.20 blue line) that was expected to be at a potential of about 0.5 V vs RHE. Instead, the CV showed an increase at 0.7 V vs RHE. It was found that the formic acid oxidation peak could be recovered by ramping the potential from 0.06 V vs RHE up to 1.1 V vs RHE multiple times (fig. 3.21).

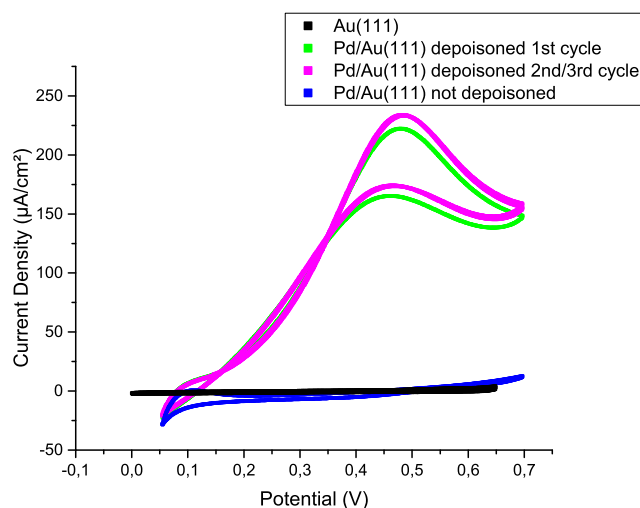


**Fig. 3.20:** Cyclic voltammogram of Pd/Au(111) in 0.1 M  $\text{H}_2\text{SO}_4$  and 0.1 M formic acid. Scan rate 20 mV/s, range 0.06 V to 0.7 V vs RHE. Blue line: CV of Pd/Au(111) before deposing procedure.

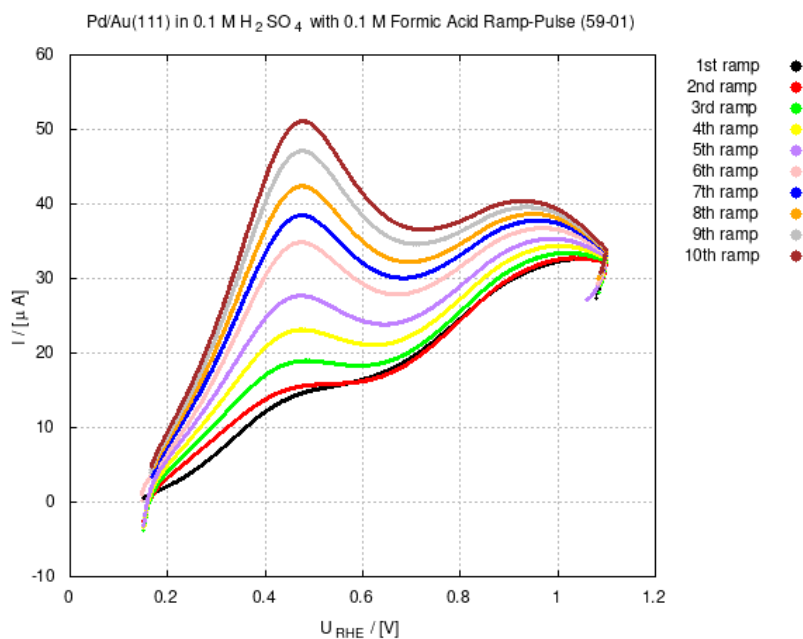


**Fig. 3.21:** Anodic scan of Pd/Au(111) in 0.1 M  $\text{H}_2\text{SO}_4$  and 0.1 M formic acid, followed by a potential jump from 1.1 V down to 0.15 V. Scan rate 20 mV/s, range 0.15 V to 1.1 V vs RHE.

It can be seen that the peak at 0.49 V vs RHE increases with each linear scan, from initial  $0.61 \mu\text{As}/\text{cm}^2$  to  $7.23 \mu\text{As}/\text{cm}^2$  after 10 scans. It also can be seen that the peak position shifts to lower potentials, from initial 0.51 V to 0.49 V after 10 scans. The formic acid oxidation charges (integral from 0.2 V to 0.7 V vs RHE) and peak positions are summarized in table 3.7 and figure 3.22. The increase of the first peak at 0.49 V vs RHE is much steeper (1185% of the initial charge after 10 scans) than the increase of the area under peak 2 at 0.95 V vs RHE (136% of the initial charge after 10 scans).

The behaviour indicates poisoning of the surface that occurs during the first CV scan which leads to a CV like the blue line in figure 3.23. By linear sweep voltammetry up to a potential of 1.1 V vs RHE, the poisoning agent gets partially desorbed from the surface. The following anodic scan shows signal for formic acid oxidation. The more poisoning agent gets desorbed from the surface, the more free surface is active for formic acid oxidation, leading to an increase in the peak signal at 0.49 V vs. RHE and leads to a potential shift down to more negative potentials.

**Tab. 3.7:** Formic acid oxidation charge and peak positions after multiple linear sweep voltammetries.

cycle	Peak1 charge [ $\mu\text{As}/\text{cm}^2$ ]	Peak1 position [V]	Peak2 charge [ $\mu\text{As}/\text{cm}^2$ ]	Peak2 position [V]
1	0.610	/	0.838	1.047
2	0.905	/	0.963	1.034
3	1.542	0.509	1.030	1.018
4	2.280	0.497	1.104	1.003
5	3.105	0.490	1.140	0.988
6	4.375	0.488	1.173	0.968
7	4.999	0.489	1.195	0.956
8	5.669	0.488	1.192	0.944
9	6.522	0.488	1.190	0.928
10	7.230	0.489	1.140	0.911

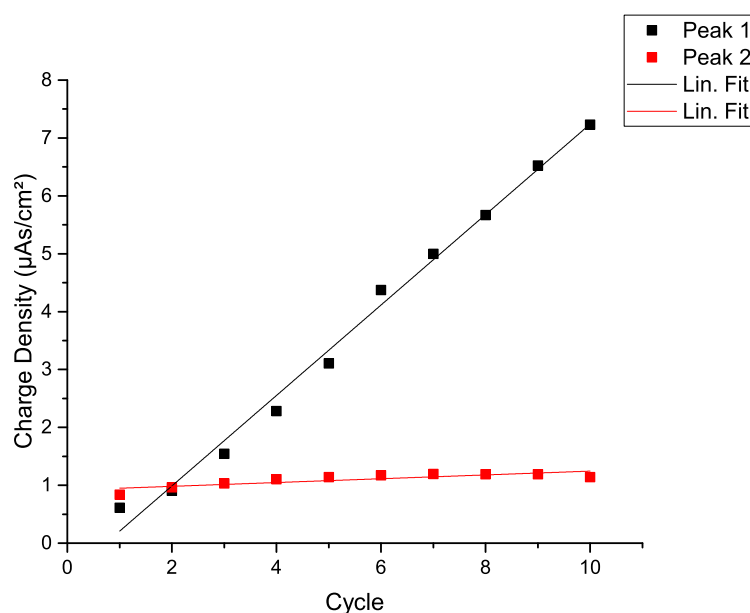


**Fig. 3.22:** Areas under peak1 (black) and peak2 (red) after different number of linear sweep voltammetry cycles.

Figure 3.20 shows the CV of Pd/Au(111) recorded after the surface depoisoning procedure. The signal of formic acid oxidation at 0.49 V vs RHE is visible in the anodic scan direction. KOLB and coworkers describe the formic acid oxidation peak at a full Pd monolayer to be at 0.44 V vs SHE.<sup>[51]</sup> They also found out that the peak position

is strongly dependent on the number of monolayers on the Au(111) surface.<sup>[51]</sup> The experiments show that Pd/Au(111) catalyzes the formic acid oxidation in contrast to pure Au(111) (fig. 3.23), but that surface poisoning can deactivate the active sites of the catalyst.

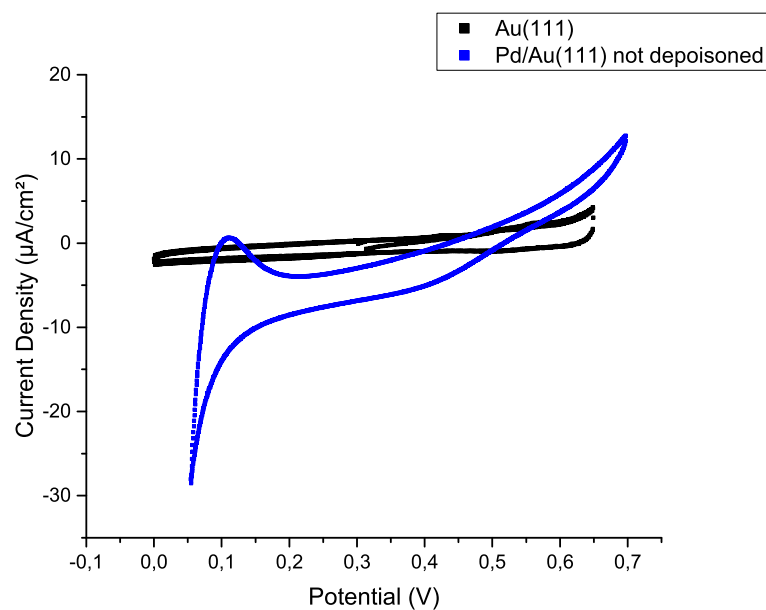


**Fig. 3.23:** CV of pristine Au(111) (black) compared to Pd/Au(111) (green). Scan rate: 25mV/s in 0.1 M H<sub>2</sub>SO<sub>4</sub> and 0.1 M formic acid.

## 3.7 Oxygen Reduction Reaction (ORR)

The ORR was followed with CV for Pd/Au(111) and Ir/Au(111) samples. Figure 3.24 shows the respective CVs in the range of 0.06 V to 0.75 V vs RHE for Pd/Au(111) (a) and Ir/Au(111) (b) respectively.

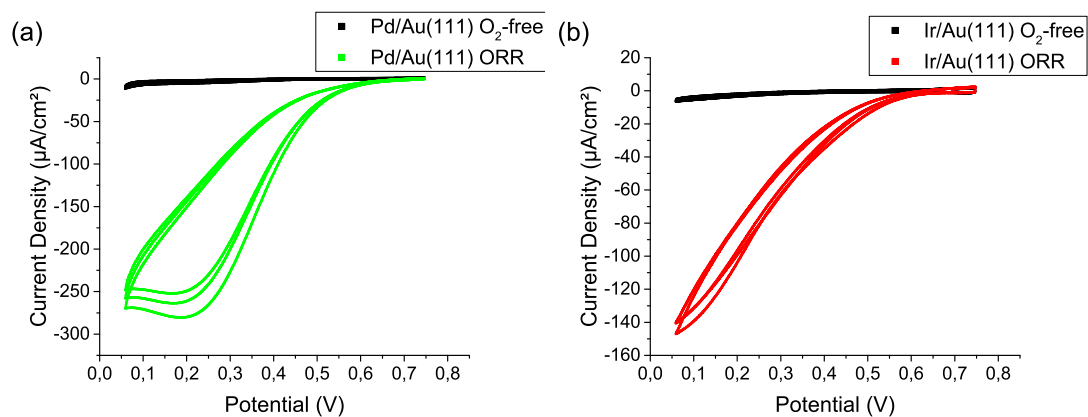


**Fig. 3.24:** Cyclic voltammogram of Pd/Au(111) (a) and Ir/Au(111) (b) in 0.1 M  $\text{H}_2\text{SO}_4$  saturated with  $\text{O}_2$  (Pd/Au(111) green, Ir/Au(111) red) and in  $\text{O}_2$ -free degassed electrolyte (black). Scan rate 20 mV/s, range 0.06 V to 0.75 V vs RHE.

The ORR can be seen in the red CVs that were performed in oxygen saturated electrolyte. For Pd/Au(111), the ORR onset is at  $0.56 \text{ V} \pm 0.06 \text{ V}$  vs RHE (lit.: Pd/Au(111) in 0.1 M  $\text{HClO}_4$   $0.8 \text{ V}$  vs RHE).<sup>[52]</sup> The ORR onset for Ir/Au(111) is  $0.49 \text{ V} \pm 0.09 \text{ V}$  vs RHE (lit.:  $0.5 \text{ V}$  vs RHE in 0.5 M  $\text{H}_2\text{SO}_4$ ).<sup>[53]</sup> The ORR onset for Pd/Au(111) is located at more positive potentials compared to the onset for Ir/Au(111) (+70 mV). Iridium is a weaker catalyst for ORR than Pd, which can be explained by its higher d-band center. The energetic level of the d-band center is directly correlated to the bonding strength of  $\text{O}_2$  to the metal surface. Higher d-band energies lead to a stronger O-O-M bonding which allows the breaking of the O-O-bond. The high binding energy also leads to a high amount of oxygenated species on the surface that are hardly desorbed.<sup>[54]</sup> A good ORR catalyst therefore needs to have a d-band energy level that is high enough to allow easy O-O-bond breaking as well as easy reduction of the M-O-species.<sup>[54]</sup>

Figure 3.25 shows the ORR for Pd/Au(111) compared to Ir/Au(111). The figure demonstrates that, in addition to the onset at higher potentials for Pd/Au(111), the ORR current density maximum is about a factor 1.9 larger for Pd/Au(111) ( $285 \mu\text{A}/\text{cm}^2$ ) than for Ir/Au(111) ( $148 \mu\text{A}/\text{cm}^2$ ).

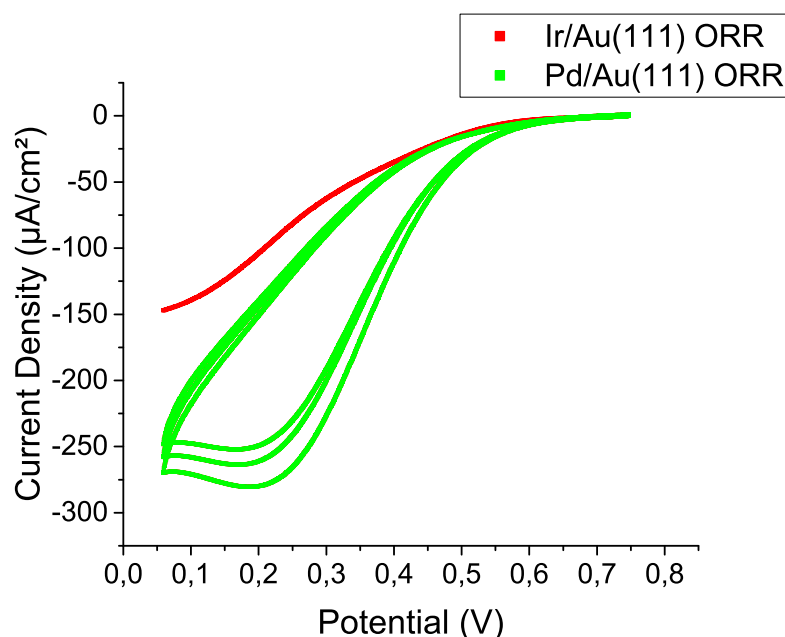


**Fig. 3.25:** Cyclic voltammogram of Pd/Au(111) (green) and Ir/Au(111) (red) in 0.1 M H<sub>2</sub>SO<sub>4</sub> saturated with O<sub>2</sub>. Scan rate 20 mV/s, range 0.06 V to 0.75 V vs RHE.

Figure 3.26 shows the ORR charge densities of Pd/Au(111) (a) and Ir/Au(111) (b) respectively for different deposition times. For Pd, the ORR activity stays nearly constant for all deposition times up to 18 s. This result indicates that an increasing Pd surface coverage does not lead to an increasing ORR activity. In accordance with the constant ORR activity with increasing Pd coverage, SHAO described a constant ORR activity for increasing number of Pd multilayers on Au(111).<sup>[52]</sup> For highly active catalyst materials, the diffusion limit of oxygen to the WE can play a role, especially in static electrode systems, to limit the ORR charges.

For Ir/Au(111), the activity increases with deposition time until a plateau is reached at about 10 s of deposition time. Since Ir/Au(111) is catalytically less active than Pd/Au(111), the diffusion limit of oxygen to the WE may be reached only for higher Ir surface coverages, which would lead to a flattening of the ORR activity curve for Ir/Au(111) at higher deposition time.

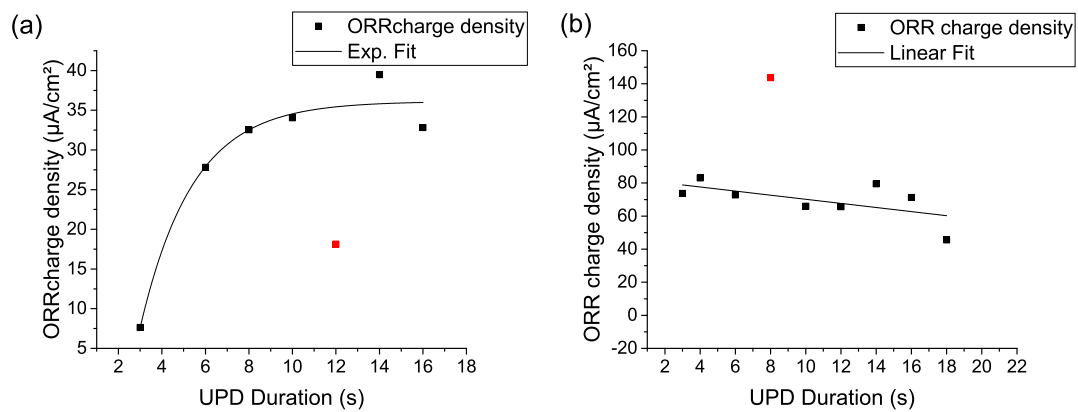


**Fig. 3.26:** ORR activity plotted against Cu deposition time for Pd/Au(111) (a) and Ir/Au(111) (b). The red marks are results that were excluded from the fit.

# Conclusion and Outlook

## 4.1 Conclusion

Pd and Ir islands were deposited on Au(111) via CuUPD and metal displacement. The resulting islands can be tuned in size and dispersion on the surface by varying the CuUPD potential and/or deposition time. The island sizes were determined by STM to be in a range from 2.3 nm to 13.8 nm for Pd/Au(111) and 10.1 nm to 30.8 nm for Ir/Au(111). The island size increases with deposition time for both deposition potentials of 0.44 V and 0.47 V vs SHE. It was shown that the surface coverage and island size depends more strongly on the deposition potential than on the deposition time. A more negative potential leads to the formation of more nuclei. The diffusion limit for copper diffusion to the electrode surface in the growth phase leads to smaller islands for more negative deposition potentials than for more positive deposition potentials.

The Pd islands show electrochemical stability in a range from -0.2 V to 0.75 V vs SHE. The start of sample degradation was observed by the HER charge in each cycle of a cyclic voltammogram.

It could be shown that Pd/Au(111) has a lower overpotential for HER of -0.06 V vs SHE compared to the overpotential for HER of Ir/Au(111) of -0.10 V vs SHE. The activity for HER can also be used to confirm the presence of Ir and Pd on the Au(111) surface. For longer deposition times of 12 s, the HER activity starts to decrease for both, Pd/Au(111) and Ir/Au(111) as a result of merging islands and therefore fewer catalytically active step sites.

A way to depoison the electrodes surface for formic acid oxidation was shown for Pd/Au(111). It was possible to increase the formic acid oxidation peak by linear sweep voltammetry to an upper limit potential of 1.1 V vs RHE. Also, the formic acid oxidation peak shifted from 0.51 V to lower potential of 0.49 V in this process.

Pd/Au(111) and Ir/Au(111) are both able to catalyze the ORR. The onset potentials for Pd/Au(111) and Ir/Au(111) were determined to be 0.56 V and 0.49 V vs RHE, respectively. Pd/Au(111) likely is a better catalyst for ORR than Ir/Au(111) because the d-band energy level is in a range that is suited to bind oxygen and break the O-O-bond and still gets easily reduced to regenerate the catalytically active sites.<sup>[54]</sup> Due to diffusion limitations, the ORR activity is constant for increasing CuUPD deposition times,

i.e. Pd coverages, for Pd/Au(111). For Ir/Au(111), the ORR activity increases with deposition time, i.e. Ir coverages, before it reaches a plateau at 10 s deposition time.

## 4.2 Outlook

First EC-TERS measurements were performed on Pd/Au(111) samples. The EC-TER spectra that were obtained did not show enhancement of the signals in the spectra and no signal for palladium oxide that were expected at the experimental conditions (PdO:  $650\text{ cm}^{-1}$ <sup>[55]</sup>, Conditions: 1.3 V vs. Pd-H, 0.1 M H<sub>2</sub>SO<sub>4</sub>, gold-tip, 632.8 nm). Figure 4.1 shows a TER spectrum obtained from Au(111) under conditions that allow defect oxidation (1.4 V vs Pd-H). The spectrum was recorded with 5 s acquisition time, using a red laser (632.8 nm, 7.92 mW). The spectrum was recorded in scan-to-point mode, the corresponding EC-STM image is shown in figure 4.2. The spectrum shows two bands around  $600\text{ cm}^{-1}$ , indicating the presence of two different gold oxide species. STAMPFL and coworkers calculated the presence of two different gold oxide bands for Au<sub>2</sub>O<sub>3</sub> and Au<sub>2</sub>O<sup>[56]</sup>. WEAVER and coworker described a single broad band at  $590\text{ cm}^{-1}$  to be the result of the presence of different gold oxide species with different geometries or hydration states.<sup>[57]</sup>

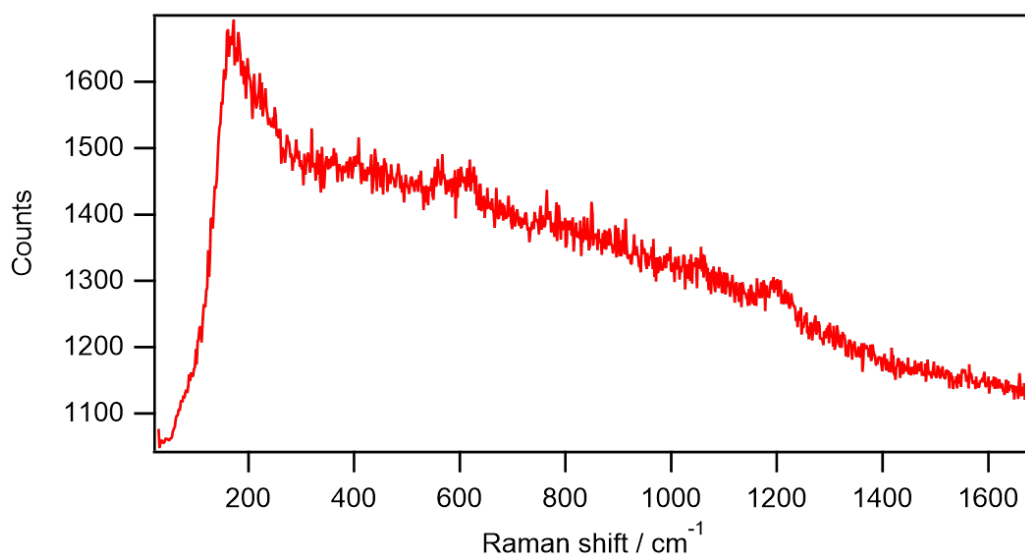


**Fig. 4.1:** TER spectrum of Au(111) recorded at 1.4 V vs Pd-H in 0.1 M H<sub>2</sub>SO<sub>4</sub> with 5 s acquisition time, 7.92 mW at 632.8 nm excitation wavelength.

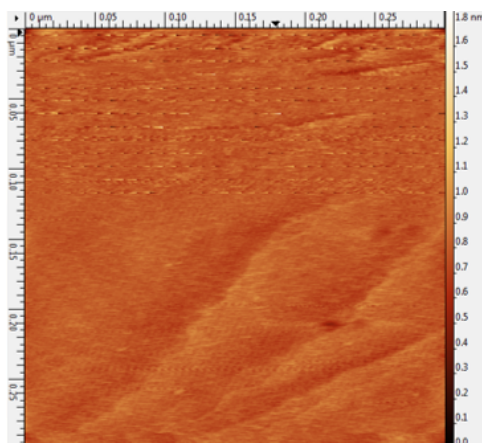


**Fig. 4.2:** EC-STM image of Au(111) recorded at 1.4V vs Pd-H in 0.1 M H<sub>2</sub>SO<sub>4</sub>, scan speed: 1 ln/s, setpoint: 1 nA.

Future EC-TERS experiments on Pd/Au(111) or Ir/Au(111) can lead to an insight into where the active catalyst sites on the samples are. With that knowledge an improvement of the catalytic activity of the samples can be done by tuning the island size and shape via CuUPD. Also, the effect of surface poisoning during formic acid oxidation can be investigated with EC-TERS. The adsorption and desorption of CO, that may be the reason for surface deactivation can be observed in EC-TER spectra and either adsorption or desorption can be triggered by changing the electrochemical conditions.

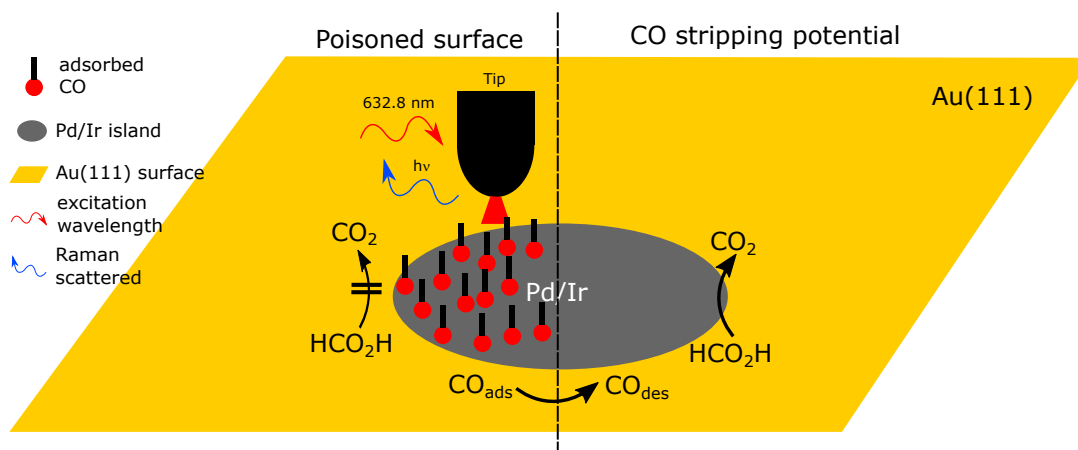


**Fig. 4.3:** Schematics of a future EC-TERS experiment to observe CO ad-/desorption on Pd/Au(111) during formic acid oxidation under potential control.

# Experimental Methodology

## 5.1 Materials

All of the following chemicals were used as purchased without further purification. The diluted acids that were used in the experiments were diluted from the respective concentrated acids by adding MilliQ-water (Merck, Type-1, Resistance:  $>18\text{ M}\Omega\text{cm}$ ). Sulfuric acid was bought from Merck ( $\text{H}_2\text{SO}_4$ , Suprapur  $>96\%$ , CAS: 7664-93-9), nitric acid was bought from Merck ( $\text{HNO}_3$ , 70%, CAS: 7697-37-2). Copper(II) sulphate pentahydrate was bought from Merck (CAS: 7758-99-8) as well as palladium chloride (Purity: 99%, CAS: 7647-10-1) and hydrogen hexachloroiridate(IV) hydrate (99.98% trace metals basis, CAS: 110802-84-1)

The gold-on-glass samples were made in-house by sputtering 10 nm chromium on a glass slide that was cut in  $1.3\text{ cm} \times 1.3\text{ cm}$  squares and then sputtering a gold layer of 200 nm thickness on top of it.

## 5.2 Preparation of the gold-on-glass samples

For the use as a substrate for the experiments of this work, the Au/Cr/glass slides were cleaned in 40% nitric acid by immersing them for 2 minutes at room temperature and rinsing with MilliQ. After that, the slides were flame-annealed using a bunsen burner flame for 5 minutes. The samples were flame-annealed to red glowing color. It was taken care that the gold layer was not damaged during the annealing by letting the surface cool down after it started glowing. This procedure was repeated multiple times during the 5 minutes overall annealing time. After the annealing, the sample was thoroughly rinsed with MilliQ water.

Directly after annealing and rinsing the sample, a gold wire (Merck, diameter: 0.5 mm, 99.997% trace metal basis) was attached to the surface using Teflon tape (High-tech-flon, thickness: 0.13 mm, hole diameter: 6 mm). The Teflon tape was cut so that it juts out only slightly by around 1 to 2 mm over the sample boundaries, just as far

**Tab. 5.1:** Properties of the non-commercial gold-on-glass samples.

<b>Dimensions</b>	1.3 cm × 1.3 cm
<b>Chrome Layer Thickness</b>	10 nm
<b>Gold Layer Thickness</b>	200 nm
<b>Tape Hole Diameter</b>	6 mm
<b>Active Surface Area</b>	0.28 mm <sup>2</sup>

enough that the two sides of the sample stuck together. Also, a hole with a diameter of 6 mm was stamped into the tape to expose a well-defined surface area to the electrolyte solution. The gold-on-glass samples were used in the electrochemical cell directly after

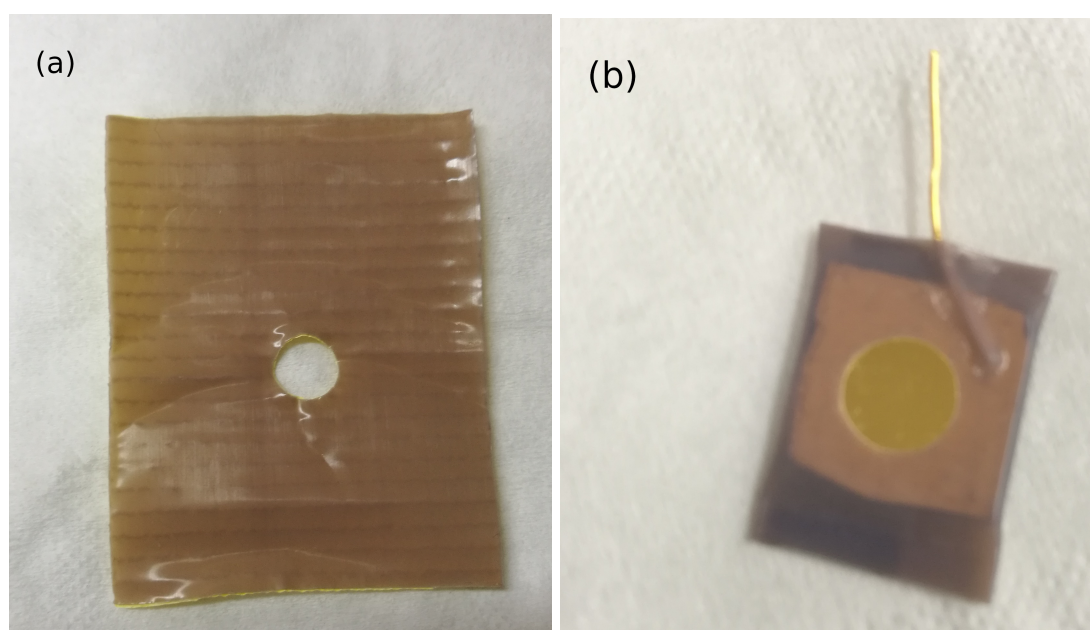


**Fig. 5.1:** (a) Teflon tape prepared for use with the gold slides. (b) Gold sample prepared for the use in the experiments.

the preparation.

## 5.3 Preparation of the counter and reference electrodes

A gold wire (Mateck, diameter: 0.5 mm, 99.997% trace metal basis) that was rolled up on one end to increase the immersed surface area was used as a counter electrode in all

experiments. Prior to connecting the wire to the potentiostat and attaching it to the cell, the counter electrode was rinsed with MilliQ water and flame-annealed with a bunsen burner flame to glowing red. Subsequently, the wire was again rinsed in MilliQ water, connected to the bipotentiostat and immersed in the electrolyte. After use, the wire was immersed in 40% nitric acid solution and rinsed in MilliQ water for cleaning.

The copper wire reference electrode for the CuUPD experiments was rinsed in MilliQ water and flame-annealed before use. After use the reference electrode was thoroughly rinsed in MilliQ water.

For all other CV experiments, a hydrogen-loaded palladium wire reference electrode was used. For the preparation, a palladium wire (Mateck, diameter: 0.5 mm, 99.9% trace metal basis) was rolled up at one end to expose a larger surface area to the electrolyte. The Pd wire was rinsed in MilliQ water and flame-annealed in a bunsen burner flame for 2 minutes. After flame-annealing, the Pd wire was again rinsed in MilliQ water. Then the wire was immersed in a 0.1 M sulfuric acid solution and connected to a potentiostat as a working electrode. A gold wire was attached as a counter electrode and a potential of 10 V was set and held for approximately 10 minutes until the hydrogen adsorption was finished. The end of the hydrogen adsorption process was indicated by the amount of gas bubbles produced on the palladium wire's surface. While there were much less bubbles on the Pd wire than on the Au wire in the beginning, the amount of bubbles on the two electrodes equalized by time, i.e. hydrogen evolution roughly corresponds to oxygen gas evolution. Afterwards the palladium wire was rinsed with MilliQ water and attached to the electrochemical cell as reference electrode.

## 5.4 Cyclic Voltammetry measurements

Cyclic Voltammetry measurements were performed using a Metrohm Autolab PGSTAT30 Potentiostat with a Metrohm Autolab Differential Electrometer Amplifier attached. NOVA (Version 2.1, Windows 7) was used as software for the electrochemical measurements. For the CV experiments, a three-electrode setup with a gold wire counter electrode, a hydrogen-loaded palladium reference electrode and a sample working electrode were used. Figure 5.2 shows the setup. The self-designed glass cell was built in-house (s. appendix 6.4) to ensure sufficient space for the electrodes and sample as well as to allow for the possibility to work under argon atmosphere.

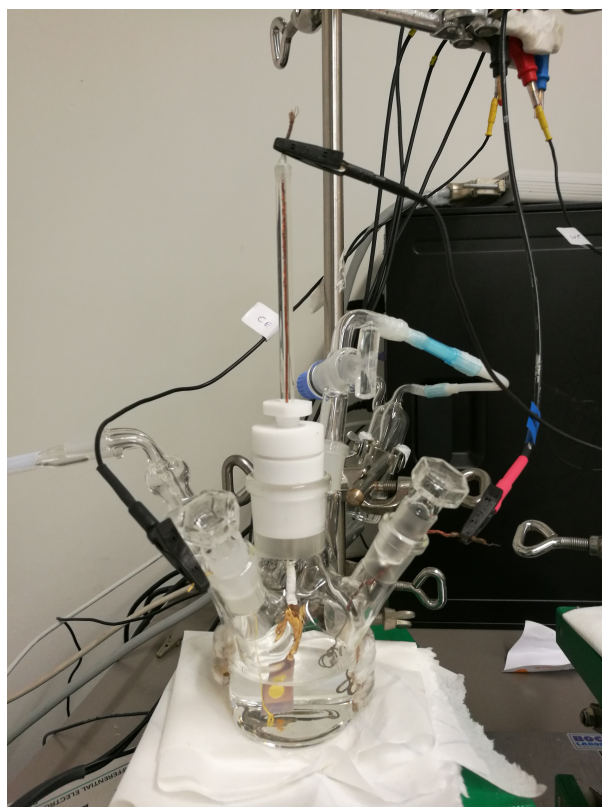


**Fig. 5.2:** Electrochemical cell used for CV experiments for characterizations.

Before each measurement, the electrolyte in the electrochemical glass cell (50 ml) was bubbled with Argon (Westfalen, Argon 6.0 T50 MFI) for 10-20 minutes. After Ar bubbling of the electrolyte, argon was continuously floated over the electrolyte's surface during the experiment to blanket the solution with an Ar atmosphere and to exclude any oxygen in the electrolyte.

The measurements were performed under the same experimental conditions, only varying the potential window and number of cycles. The scan speed was 25 mV/s (unless stated otherwise) using linear scan with a potential interval of 0.00244 V/s that determines the number of data points recorded during the measurement. If not stated otherwise, every measurement was done by performing 3 full cycles.

For CuUPD experiments, a second glass cell was used in the same way as the one for characterization measurements but with the use of a copper wire reference electrode instead of a hydrogen-loaded palladium wire. The Cu reference electrode is in equilibrium with the Cu ions in solution, i.e. below 0 V vs Cu/Cu<sup>2+</sup>, bulk deposition is initiated at the Au working electrode.

Before the start of each experiment, the glassware was cleaned by boiling in nitric acid (40% solution) for 1 hour. After boiling, the solution was allowed to cool down. Afterwards, the glassware was rinsed with MilliQ water multiple times and filled up with MilliQ. The MilliQ water inside the cells and other glassware was boiled for 10 minutes and the glassware was again rinsed in fresh MilliQ water. This procedure was repeated three times to ensure the glassware was clean and free from nitric acid residues. The glassware used in the experiments that were made in Alicante was cleaned by storing it in potassium permanganate over night. After that, the glassware was washed in a hydrogen peroxide solution, rinsed in MilliQ water multiple times and filled up with MilliQ water. The MilliQ water inside the cells and other glassware was boiled for 10 minutes and the glassware was again rinsed in fresh MilliQ water. This procedure was repeated three times to ensure the glassware was clean and free from potassium permanganate residues.

## 5.5 CuUPD

For the CuUPD, a copper containing electrolyte was prepared from copper sulphate (12.5 mg in 50 ml H<sub>2</sub>O) and sulfuric acid (2.77 ml in 50 ml H<sub>2</sub>O) to obtain a 1 mM solution of CuSO<sub>4</sub> in 0.1 M H<sub>2</sub>SO<sub>4</sub>. All CuUPD experiments were performed according to the same experimental procedure described in the following. Only the applied potential and/or deposition time were varied.

After bubbling argon through the electrolyte for 10 minutes, the electrolyte solution was blanketed with Ar. The CuUPD was performed by applying a start potential of 0.5 V vs Cu/Cu<sup>2+</sup> to the electrode and holding it for 15 seconds to let the system reach equilibrium. After that, the potential was set to the target potential of 0.12 V vs Cu/Cu<sup>2+</sup> (0.15 V respectively) and held for the given time. Right after that, the potential was set to open circuit potential, the cell was shut off and the working electrode removed and rinsed in MilliQ water.

## 5.6 Metal Displacement

For the galvanic metal displacement, 10 mM aqueous solutions of palladium(II) chloride (35.5 mg in 20 ml H<sub>2</sub>O) and hydrogen iridium hexachloride (81.3 mg in 20 ml H<sub>2</sub>O) were prepared and stored under oxygen exclusion. After the CuUPD, the Cu islands on

Au samples were rinsed with MilliQ water and directly immersed into the metal solution (either Pd or Ir containing) for 10 seconds. The samples were again carefully rinsed carefully with MilliQ water.

## 5.7 Scanning Tunneling Microscopy

Scanning tunneling microscopy was performed using a Keysight technologies GmbH (former Agilent) 5500 Atomic Force Microscope in STM mode. All STM measurements were performed in ambient air at room temperature. For STM tip preparation, a Pt/Ir wire (80:20, Mateck, diameter: 0.5 mm) was torn with a plier. The samples were mounted on the STM holder and fixed with a Teflon piece. The gold wire attached to each sample was used to connect the sample to the STM. Measurements were performed using the Software PicoView (Keysight, Windows 7) in STM mode.

The post processing of the images was performed using the free-for-use software Gwyddion (Version 2.53 64-bit, Windows 10). All raw files obtained from the STM instrument were plain leveled automatically by the software and background subtracted using a second-order polynomial. Afterwards, the rows of the STM image were automatically aligned using the line median as representative height.

## 5.8 Electrochemical tip-enhanced Raman spectroscopy

For EC-TERS, gold tips were used as EC-STM tips. The tips were cut from a gold wire (Mateck, Diameter: 0.25 mm, 99.997% trace metal basis) to a length of about 1.5 cm. Each piece of Au wire was subsequently rinsed with ethanol and MilliQ. The wire pieces were electrochemically etched to form a well-formed, symmetrical tip apex in a 1:1 mixture of ethanol and HCl. After etching, the tips were rinsed with MilliQ to remove any residuals and then coated with a thin layer of Zapon (CLOU, Germany). The coating prevents faradaic currents from floating between the tip and the electrolyte solution.

The EC-TERS setup is house-built and consists of a commercially available STM (Keysight 5420) and a red laser (HeNe, REO LSPR-3501, 632.8 nm, linearly polarized) with a

maximal output power of 35 mW. The instrument is mounted on a vibration-damped table (CleanTop, TMC) to avoid any vibrations during the measurements. The optical mirrors were purchased from ThorLabs. A series of grey filter and mirrors is followed by a filter wheel (FW2012W) with optical density filters in the range of 0.1 and 1.3 to be able to control the laser power of the incident beam. A dichroic long-pass beam splitter (Semrock RazorEdge Dichroic LPD02-633RU-25) in the detection path with a cut-off value of  $156\text{ cm}^{-1}$  filters out the elastic Rayleigh scattering. The incident beam is focused using a 50x long working distance objective (Olympus, working distance: 10.6 mm, numeric aperture: 0.5), also used to collect the scattered light. A flippable beam splitter allows the use of a CMOS camera (MC 1362, Mikrottron) to focus the laser beam on the tip apex. The collected scattering light passes a long pass edge filter (Semrock RazorEdgeultra steep long pass edge filter LP02-633RE-25) before entering the spectrograph. The spectrograph (Horiba iHR550) has three gratings (600, 1200 and 1800 g/mm) allowing for the adjustment of the spectral resolution. The detector is a CCD camera (Horiba Symphony II) cooled with fluid nitrogen. A scheme of the setup is shown in figure 5.3.

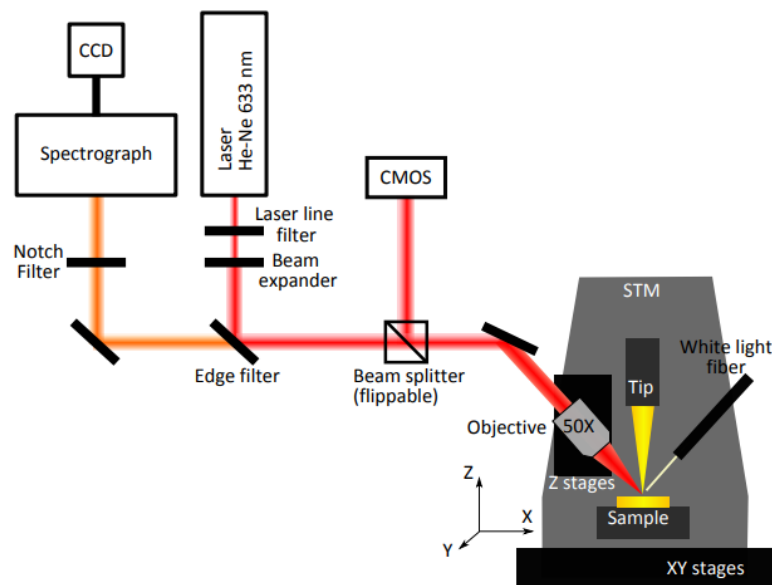


**Fig. 5.3:** Scheme of the EC-TERS setup used in the experiments. Red: Incident beam path. Orange: Detection beam path.<sup>[58]</sup>

The laser beam was focused on the tip with the help of a white light (fiber, KL 1600 LED, Schott) image recorded by the CMOS camera placed opposite to the objective. The shadow of the tip with respect to the laser position can be seen using the CMOS camera. Using the x,y,z piezo stage, the laser beam can be focused on the STM-tip apex. First, the focusing was done in air, but because of the refractive index of the electrolyte when using the setup under EC conditions, the focusing had to be adjusted with great care after changing to EC conditions.

The electrochemical cell used for this experiment was home-built and it is shown in figure 5.4. It consists of a Kel-F body and a glass window that is glued to the body using a UV-light (Loctite 3321). The sample is mounted to the cell using an O-ring to prevent leakage of the electrolyte.

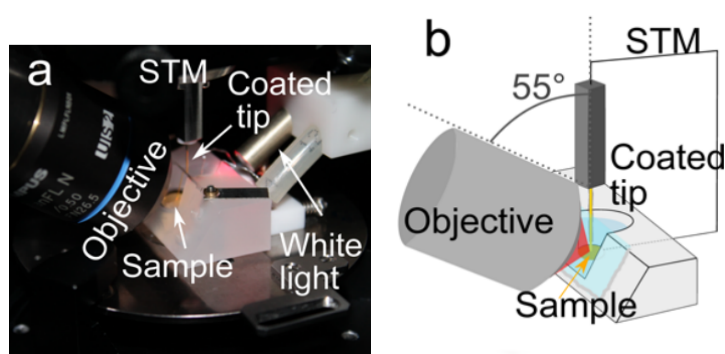


**Fig. 5.4:** Left: Image of the TERS cell used for the experiments mounted in the setup. Right: scheme of the TERS cell used in the experiments.<sup>[58]</sup>

# Bibliography

- [1]M. Zeng, Y. Li, *Journal of Materials Chemistry A* **2015**, *3*, 14942–14962.
- [2]C. Zhang, X. Shen, Y. Pan, Z. Peng, *Frontiers in Energy* **2017**, *11*, 268–285.
- [3]D. V. Esposito, S. T. Hunt, Y. C. Kimmel, J. G. Chen, *Journal of the American Chemical Society* **2012**, *134*, 3025–3033.
- [4]Y. Cheng, S. P. Jiang, *Progress in Natural Science: Materials International* **2015**, *25*, 545–553.
- [5]D. V. Esposito, J. G. Chen, *Energy and Environmental Science* **2011**, *4*, 3900–3912.
- [6]C. Rakousky, G. P. Keeley, K. Wippermann, M. Carmo, D. Stolten, *Electrochimica Acta* **2018**, *278*, 324–331.
- [7]J. C. C. Gómez, R. Moliner, M. J. Lázaro, *Catalysts* **2016**, *6*, 130.
- [8]Z.-C. Zeng, S.-C. Huang, D.-Y. Wu, et al., *Journal of the American Chemical Society* **2015**, *137*, 11928–11931.
- [9]R. Zhang, Y. Zhang, Z. C. Dong, et al., *Nature* **2013**, *498*, 82–86.
- [10]S. Lee, R. Hoffmann, *Journal of the American Chemical Society* **2002**, *124*, 4811–4823.
- [11]R. Addou, L. Colombo, R. M. Wallace, *ACS Applied Materials and Interfaces* **2015**, *7*, 11921–11929.
- [12]U. Müller, *Anorganische Strukturchemie, Vol. 6*, Vieweg+Teubner, **2008**.
- [13]E. Budevski, G. Staikov, W. Lorenz, *Electrochemical phase formation and growth*, VCH, Weinheim, **1996**.
- [14]C. Solar, A. G. Blanco, A. Vallone, K. Sapag, *Natural Gas* **2010**, 205–244.
- [15]U. Aschauer, Y. He, H. Cheng, et al., *Journal of Physical Chemistry C* **2010**, *114*, 1278–1284.
- [16]Y. Wang, H. Sun, S. Tan, H. F. et al., *Nature Communications* **2013**, *4*, 2214.
- [17]T. Fujita, P. Guan, K. McKenna, X. Lang, A. H. et al., *Nature Materials* **2012**, *11*, 775–780.

- [18]V. M. Hallmark, S. Chiang, J. F. Rabolt, J. D. Swalen, R. J. Wilson, *Physical Review Letters* **1987**, *59*, 2879–2884.
- [19]V. Repaina, J. M. Berroira, S. Rousseta, J. Lecoeurb, *Surface Science* **2000**, *447*, 152–156.
- [20]W. Haiss, D. Lackey, J. K. Sass, *Journal of Chemical Physics* **1991**, *95*, 2193–2196.
- [21]A. I. Nazri, Sudiby, N. I. Basir, M. N. Murat, *IOP Conference Series: Materials Science and Engineering* **2019**, *478*, 1–8.
- [22]J. Tang, M. Petri, L. A. Kibler, D. M. Kolb, *Electrochimica Acta* **2005**, *51*, 127–132.
- [23]C. R. K., R. D. Trivedi, *Coordination Chemistry Reviews* **2005**, *249*, 613–631.
- [24]D. Gokcen, S.-E. Bae, S. R. Brankovic, *Electrochimica Acta* **2011**, *56*, 5545–5553.
- [25]N. Mayet, K. Servat, K. B. Kokoh, T. W. Napporn, *Surfaces* **2019**, *2*, 257–276.
- [26]A. Papaderakis, I. Mintsouli, J. Georgieva, S. Sotiropoulos, *Catalysts* **2017**, *7*, 80–114.
- [27]J. K. Norskov, J. Rossmeisl, A. Logadottir, et al., *Journal of Physical Chemistry B* **2004**, *108*, 17886–17892.
- [28]J. Wu, H. Yang, *Accounts of Chemical Research* **2013**, *46*, 1848–1857.
- [29]R. Wang, Z. Chen, N. Hu, et al., *ChemElectroChem* **2018**, *5*, 1–20.
- [30]*Catalysis: Concepts and Green Applications*, Vol. 99, (Ed.: G. Rothenberg), Wiley-VCH, Weinheim, **2008**.
- [31]A. Karpenko, R. Leppelt, V. Plzak, et al., *Topics in Catalysis* **2007**, *44*, 183–198.
- [32]H. Zea, K. Lester, A. K. Datye, et al., *Applied Catalysis A: General* **2005**, *282*, 237–245.
- [33]E. H. K. Stelzer, *Nature* **2002**, *417*, 806–807.
- [34]C. Kisielowski, B. Freitag, M. Bischoff, H. van Lin, *Microscopy and Microanalysis* **2008**, *14*, 469–477.
- [35]C. J. Chen, *Introduction to scanning tunneling microscopy*, Vol. 1, Oxford University Press, New York, **1993**.
- [36]I. de Wolf, *Semiconductor Science and Technology* **1996**, *11*, 139.
- [37]J. Wessel, *Journal of the Optical Society of America B: Optical Physics* **1985**, *2*, 1538–1541.
- [38]R. M. Stockle, Y. D. Suh, V. Deckert, R. Zenobi, *Chemical Physics Letters* **2000**, *318*, 131–136.
- [39]M. Fleischmann, P. J. Hendra, A. J. McQuillan, *Chemical Physics Letters* **1974**, *26*, 163–166.
- [40]G. C. Schatz, R. P. V. Duyne, *Surface Science* **1980**, *101*, 425–438.
- [41]J. H. K. Pfisterer, K. F. Domke, *Current Opinion in Electrochemistry* **2018**, *8*, 96–102.

- [42]N. M. Sabanes, T. Ohto, D. Andrienko, Y. Nagata, K. F. Domke, *Angewandte Chemie International Edition* **2017**, *56*, 9796–9801.
- [43]J. H. K. Pfisterer, K. F. Domke, **2019**, submitted.
- [44]J.-H. Zhong, X. Jin, L. Meng, et al., *Nature Nanotechnologies* **2017**, *12*, 132–136.
- [45]A. Kuzume, E. Herrero, J. M. Feliu, R. J. Nicholsa, D. J. Schiffrin, *Physical Chemistry Chemical Physics* **2004**, *6*, 619–625.
- [46]E. Herrero, L. J. Buller, H. D. Abruna, *Chemical Reviews* **2001**, *101*, 1897–1930.
- [47]*CRC Handbook of chemistry and physics, Vol. 99*, (Eds.: W. M. Haynes, D. R. Lide, T. J. Bruno), CRC Press, Boca Raton, Florida, **2018**.
- [48]E. Garfias-Garciaa, M. Palomar-Pardavéb, M. Romero-Romoc, M. T. Ramírez-Silvad, N. Batinae, *ECS Transactions* **2007**, *3*, 35–43.
- [49]A. MEI-Aziz, L. AKibler, *Journal of Electroanalytical Chemistry* **2002**, *534*, 107–114.
- [50]T. Wang, L. Liu, Z. Zhu, et al., *Energy and Environmental Science* **2013**, *6*, 625–633.
- [51]M. Baldauf, D. M. Kolb, *Journal of Physical Chemistry* **1996**, *100*, 11375–11381.
- [52]M. Shao, *Journal of Power Sources* **2011**, *196*, 2433–2444.
- [53]E. Antolini, *ACS Catalysis* **2014**, *4*, 1426–1440.
- [54]F. H. B. Lima, J. Zhang, M. H. Shao, et al., *Journal of Physical Chemistry C* **2007**, *111*, 404–410.
- [55]W. H. Weber, R. J. Baird, G. W. Graham, *Journal of Raman Spectroscopy* **1988**, *19*, 239–244.
- [56]A. MEI-Aziz, L. AKibler, *Physical Reviews B* **2007**, *75*, 1–8.
- [57]J. Desilvestro, M. J. Weaver, *Journal of Electroanalytical Chemistry* **1986**, *209*, 377–386.
- [58]N. M. Sabanes, L. M. A. Driessen, K. F. Domke, *Analytical Chemistry* **2016**, *88*, 7108–7114.

# Appendix

## 6.1 Pd/Au(111)

### 6.1.1 3 s, sweep 0.15 V

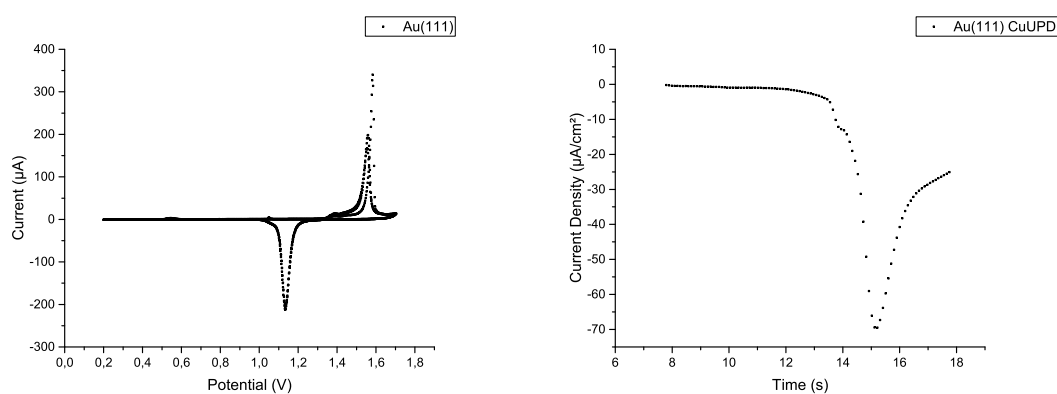


**Fig. 6.1:** (left) CV of pristine Au(111). (right) CuUPD of Pd/Au(111) (3 s CuUPD deposition time, scanned from 0.4 V to 0.15 V vs Cu/Cu<sup>2+</sup> CuUPD deposition potential).

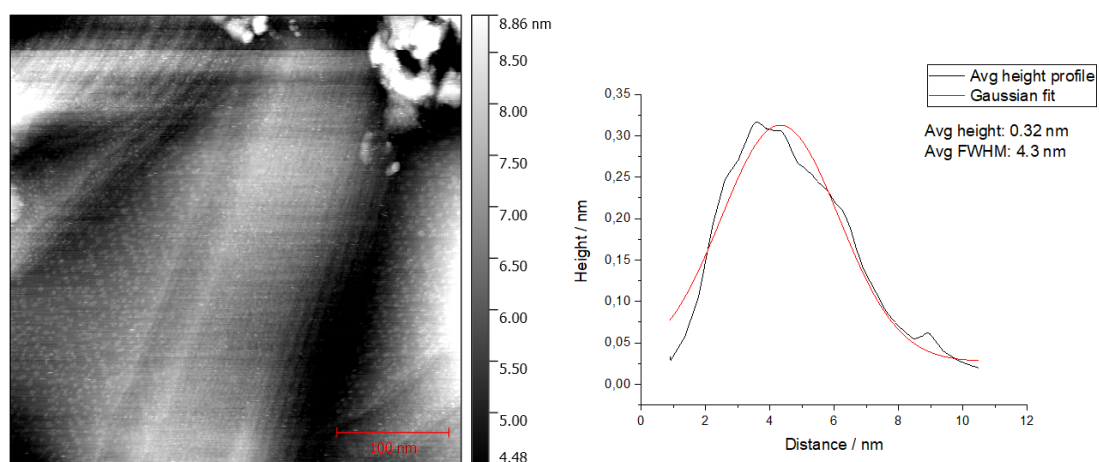


**Fig. 6.2:** (left) STM image of Pd/Au(111) after CuUPD 3 s scan from 0.4 V to 0.15 V. (right) Average Pd island size.

## 6.1.2 3 s, 0.12 V

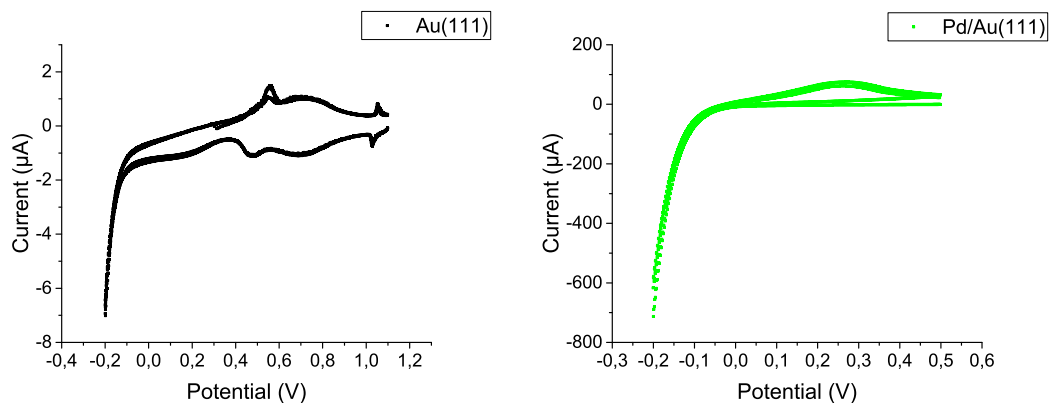


**Fig. 6.3:** (left) CV of pristine Au(111). (right) CV of Pd/Au(111) (3 s CuUPD deposition time, 0.12 V vs Cu/Cu<sup>2+</sup> CuUPD deposition potential). Immersion potential: 0.3 V vs SHE, scan rate: 25 mV/s.

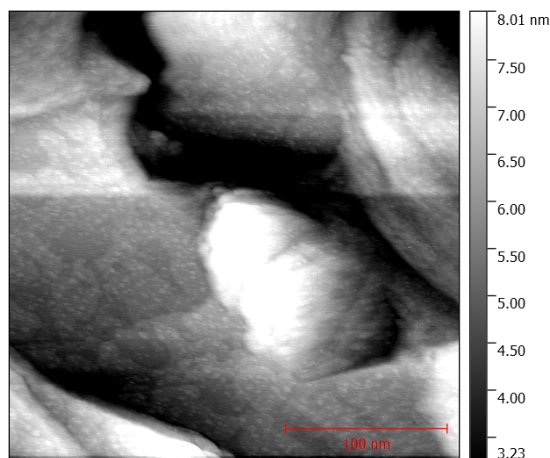


**Fig. 6.4:** STM image of Pd/Au(111) after CuUPD 3 s deposition time with 0.12 V deposition potential.

### 6.1.3 5 s, 0.15 V

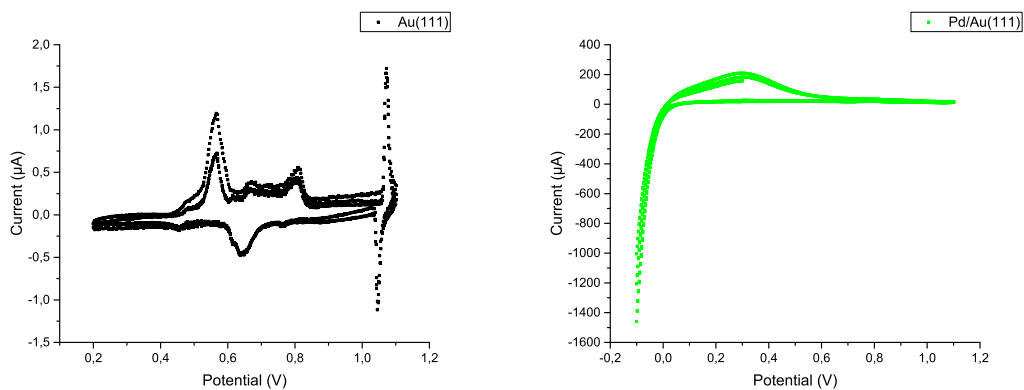


**Fig. 6.5:** (left) CV of pristine Au(111). (right) CV of Pd/Au(111) (5 s CuUPD deposition time, 0.15 V vs Cu/Cu<sup>2+</sup> CuUPD deposition potential). Immersion potential: 0.3 V vs SHE, scan rate: 25 mV/s.

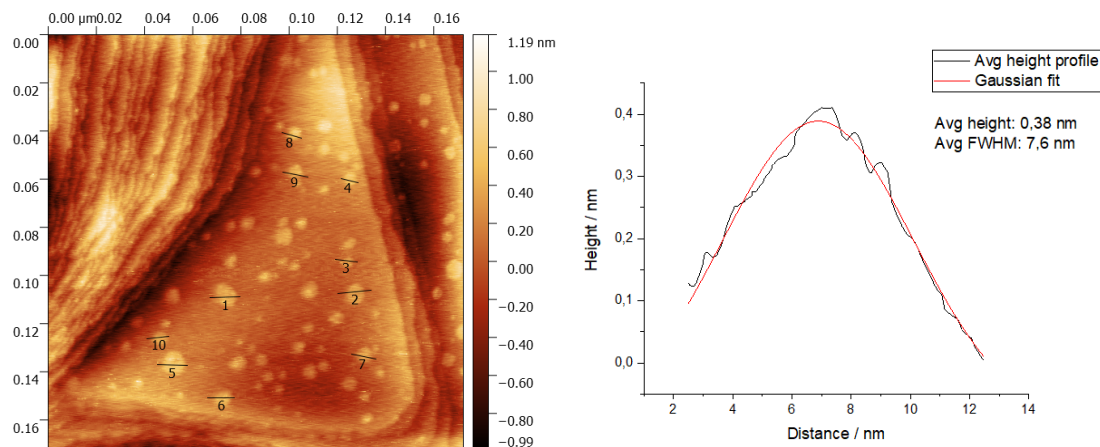


**Fig. 6.6:** (left) STM image of Pd/Au(111) after CuUPD 5 s deposition time with 0.15 V deposition potential. (right) Average Pd island size.

## 6.1.4 9 s, 0.15 V

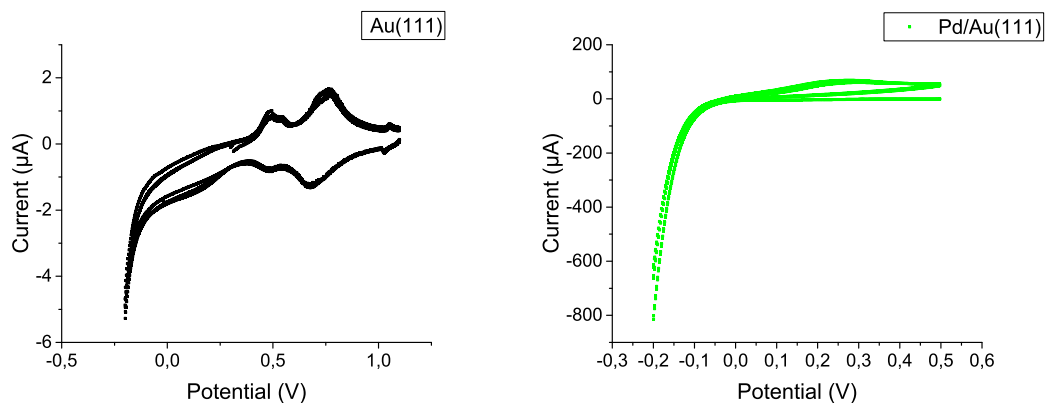


**Fig. 6.7:** (left) CV of pristine Au(111). (right) CV of Pd/Au(111) (9 s CuUPD deposition time, 0.15 V vs Cu/Cu<sup>2+</sup> CuUPD deposition potential). Immersion potential: 0.3 V vs SHE, scan rate: 25 mV/s.

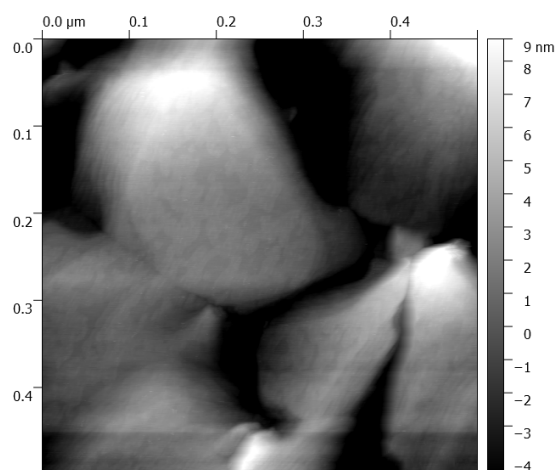


**Fig. 6.8:** STM image of Pd/Au(111) after CuUPD 9 s deposition time with 0.15 V deposition potential.

## 6.1.5 10 s, 0.15 V

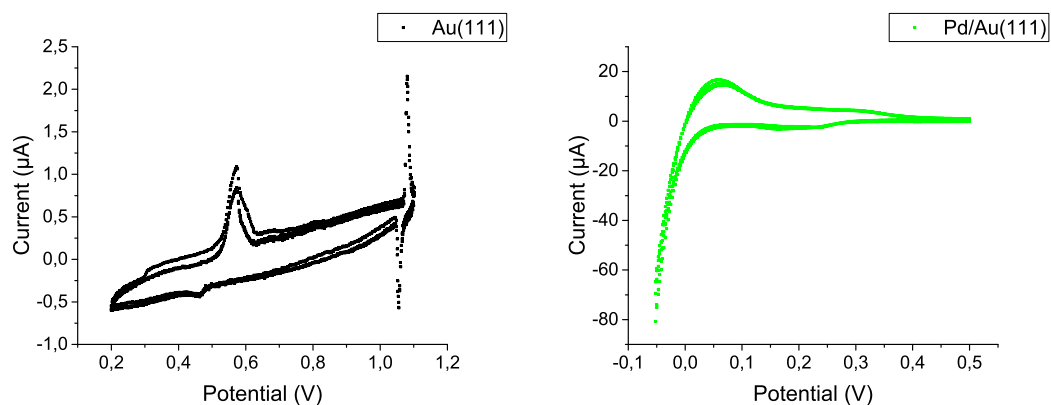


**Fig. 6.9:** (left) CV of pristine Au(111). (right) CV of Pd/Au(111) (10 s CuUPD deposition time, 0.15 V vs Cu/Cu<sup>2+</sup> CuUPD deposition potential). Immersion potential: 0.3 V vs SHE, scan rate: 25 mV/s.

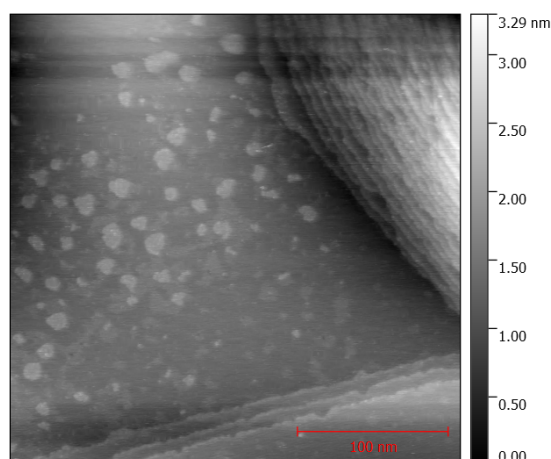


**Fig. 6.10:** STM image of Pd/Au(111) after CuUPD 10 s deposition time with 0.15 V deposition potential.

## 6.2 Ir/Au(111)

### 6.2.1 3 s, 0.15 V

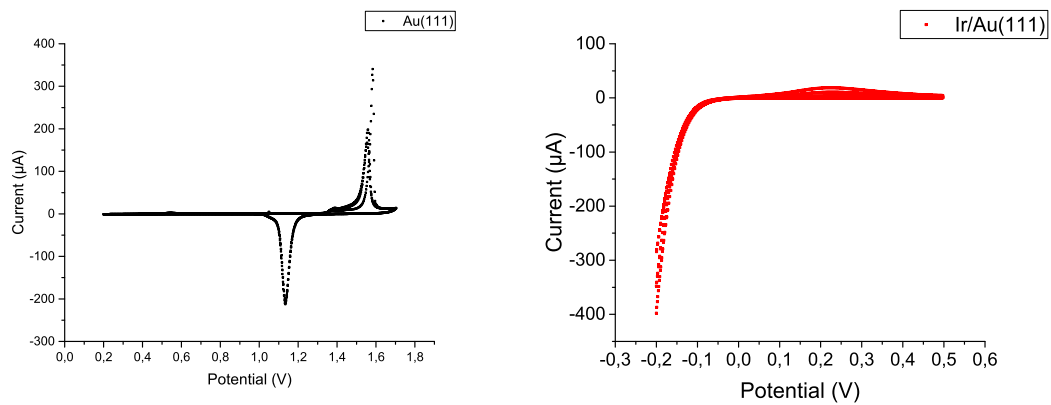


**Fig. 6.11:** (left) CV of pristine Au(111). (right) CV of Ir/Au(111) (3 s CuUPD deposition time, 0.15 V vs Cu/Cu<sup>2+</sup> CuUPD deposition potential). Immersion potential: 0.3 V vs SHE, scan rate: 25 mV/s.

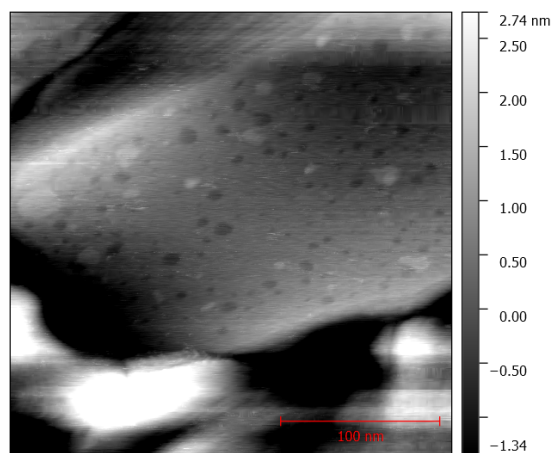


**Fig. 6.12:** STM image of Ir/Au(111) after CuUPD 3 s deposition time with 0.15 V deposition potential.

## 6.2.2 6 s, 0.15 V

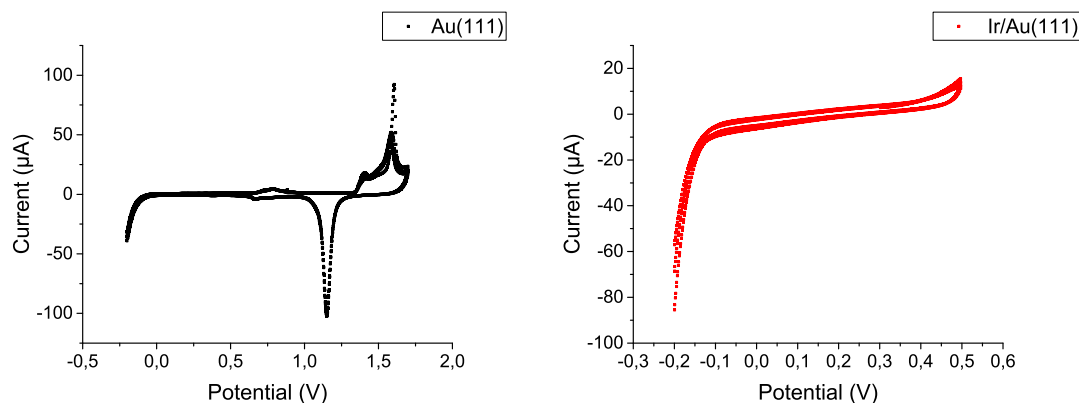


**Fig. 6.13:** (left) CV of pristine Au(111). (right) CV of Ir/Au(111) (6 s CuUPD deposition time, 0.15 V vs Cu/Cu<sup>2+</sup> CuUPD deposition potential). Immersion potential: 0.3 V vs SHE, scan rate: 25 mV/s.

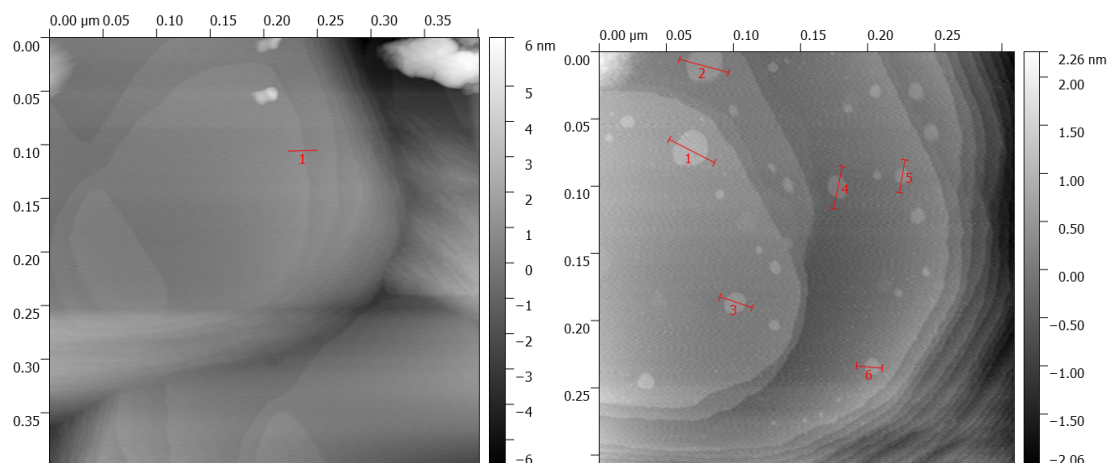


**Fig. 6.14:** (left) STM image of pristine Au(111). (right) STM image of Ir/Au(111) after CuUPD 6 s deposition time with 0.15 V deposition potential. Immersion potential: 0.3 V vs SHE, scan rate: 25 mV/s.

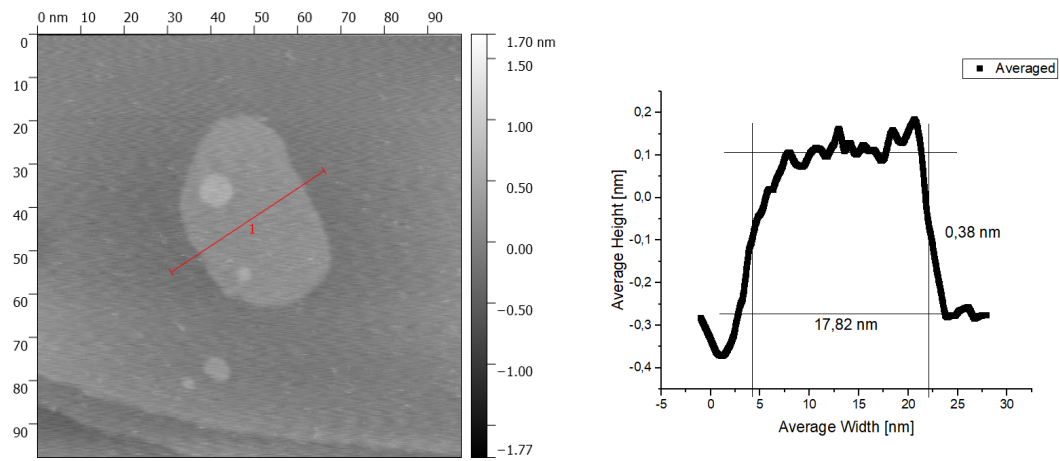


**Fig. 6.15:** (left) STM image Ir/Au(111). (right) Average Ir island size.

### 6.2.3 9 s, 0.15 V

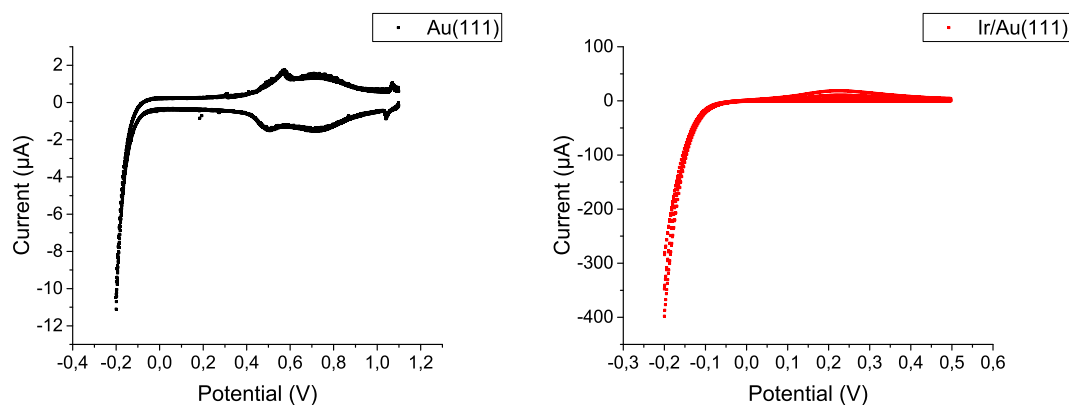


**Fig. 6.16:** (left) CV of pristine Au(111). (right) CV of Ir/Au(111) (9 s CuUPD deposition time, 0.15 V vs Cu/Cu<sup>2+</sup> CuUPD deposition potential). Immersion potential: 0.3 V vs SHE, scan rate: 25 mV/s.

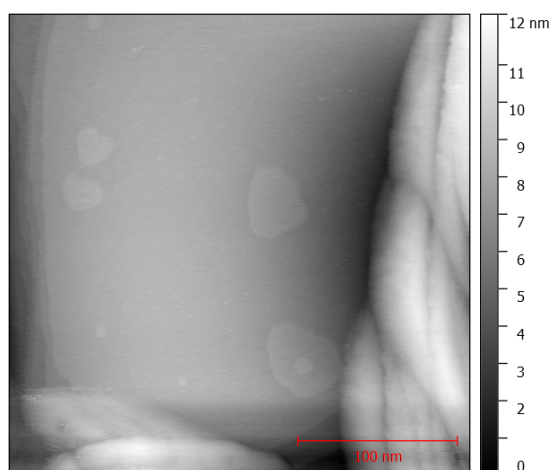


**Fig. 6.17:** STM image of Ir/Au(111) after CuUPD 9 s deposition time with 0.15 V deposition potential.

## 6.2.4 12 s, 0.15 V

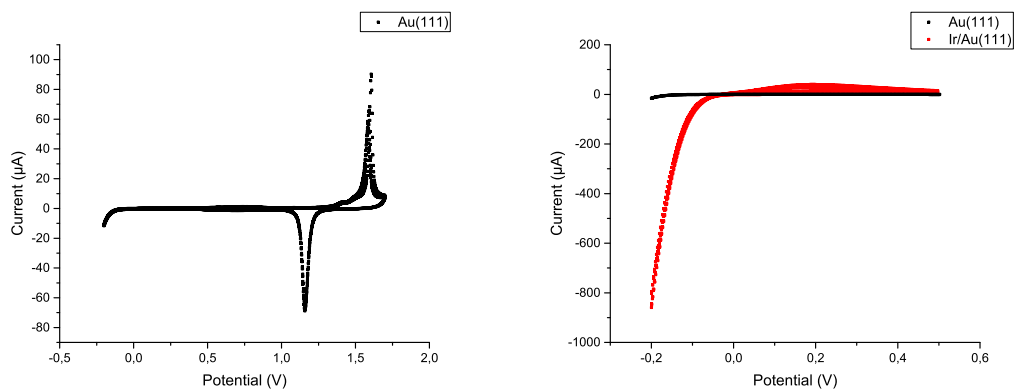


**Fig. 6.18:** (left) CV of pristine Au(111). (right) CV of Ir/Au(111) (12 s CuUPD deposition time, 0.15 V vs  $\text{Cu}/\text{Cu}^{2+}$  CuUPD deposition potential). Immersion potential: 0.3 V vs SHE, scan rate: 25 mV/s.

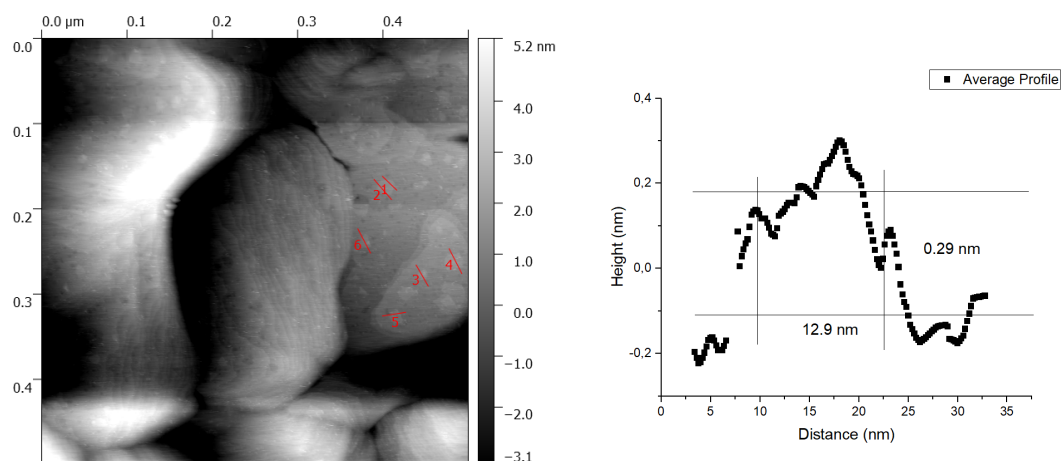


**Fig. 6.19:** (left) STM image of Ir/Au(111) after CuUPD 12 s deposition time with 0.15 V deposition potential. (right) Average Ir island size.

## 6.3 X-ray photoelectron spectroscopy

### 6.3.1 Pd/Au(111)

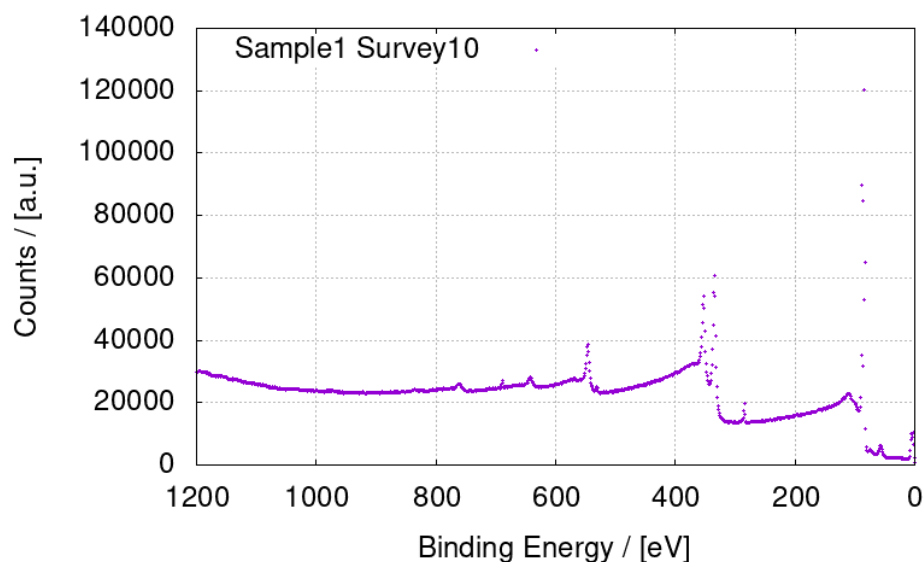


**Fig. 6.20:** Full range (0 - 1200 eV binding energy) XPS spectrum of Pd/Au(111).

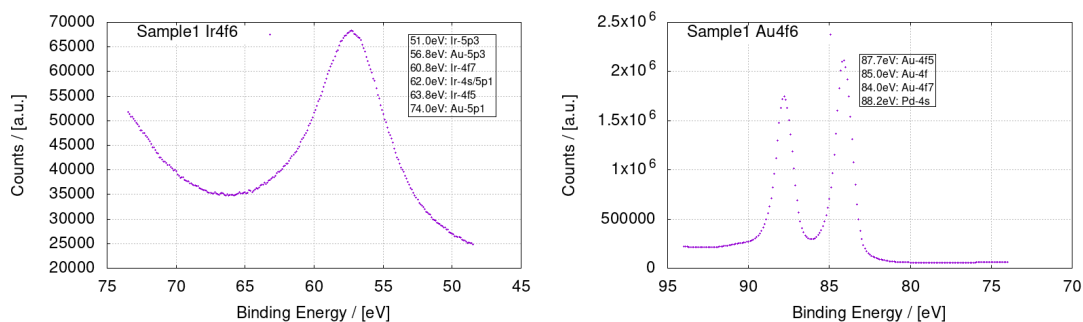


**Fig. 6.21:** (left) XPS spectrum (45 - 75 eV binding energy) of Pd/Au(111). (right) XPS spectrum (70 - 95 eV binding energy) of Pd/Au(111).

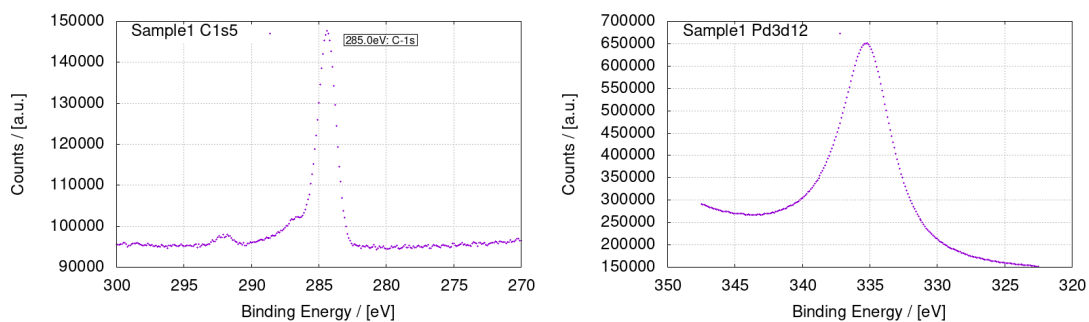


**Fig. 6.22:** (left) XPS spectrum (270 - 300 eV binding energy) of Pd/Au(111). The spectrum shows only low counts for carbon on the sample. (right) XPS spectrum (320 - 350 eV binding energy) of Pd/Au(111).

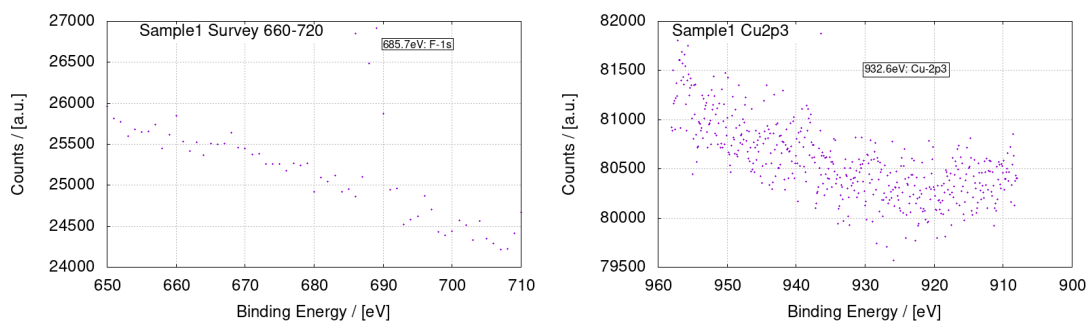


**Fig. 6.23:** (left) XPS spectrum (650 - 710 eV binding energy) of Pd/Au(111). (right) XPS spectrum (900 - 960 eV binding energy) of Pd/Au(111). The spectrum shows no residues of copper left from CuUPD.

## 6.3.2 Ir/Au(111)

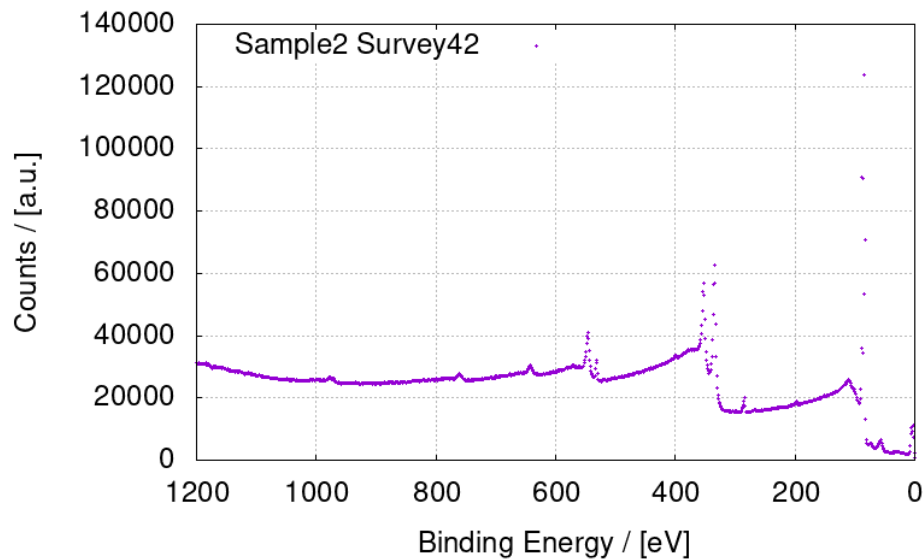


**Fig. 6.24:** Full range (0 - 1200 eV binding energy) XPS spectrum of Ir/Au(111).

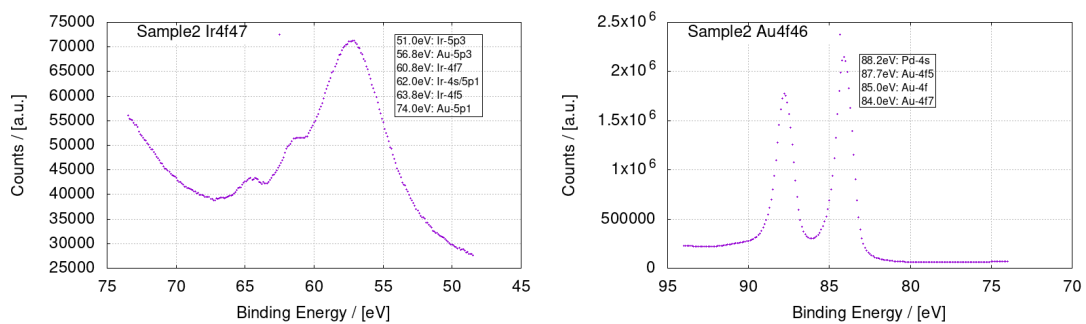


**Fig. 6.25:** (left) XPS spectrum (48 - 74 eV binding energy) of Ir/Au(111) showing signals for iridium. (right) XPS spectrum (74 - 94 eV binding energy) of Ir/Au(111).

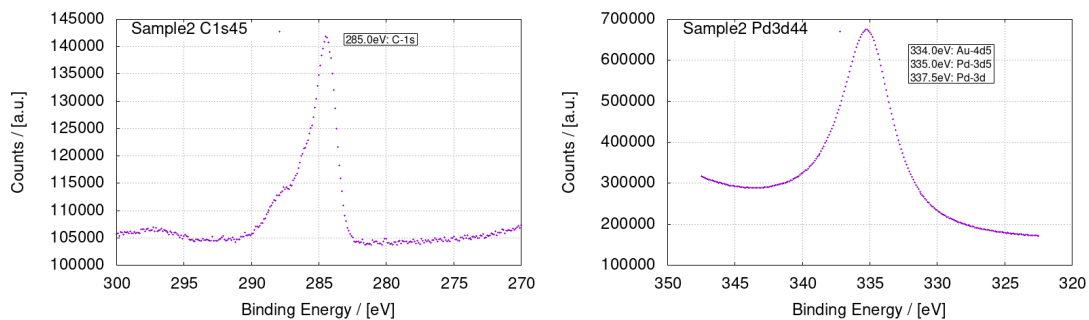


**Fig. 6.26:** (left) XPS spectrum (270 - 300 eV binding energy) of Ir/Au(111). The spectrum shows only low counts for carbon on the sample. (right) XPS spectrum (320 - 350 eV binding energy) of Ir/Au(111).

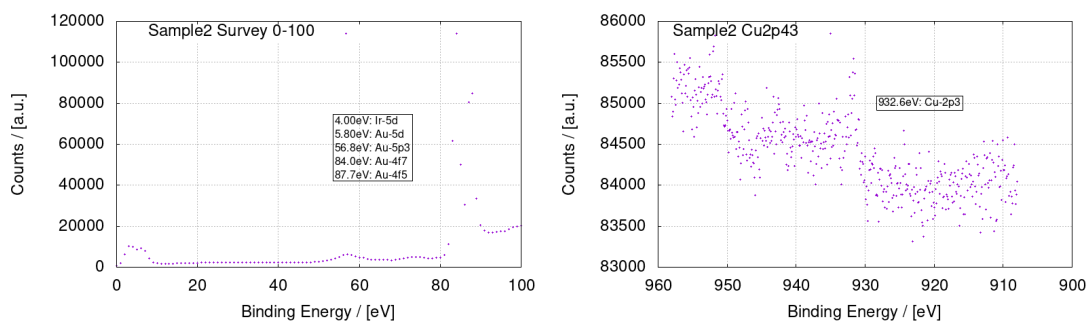
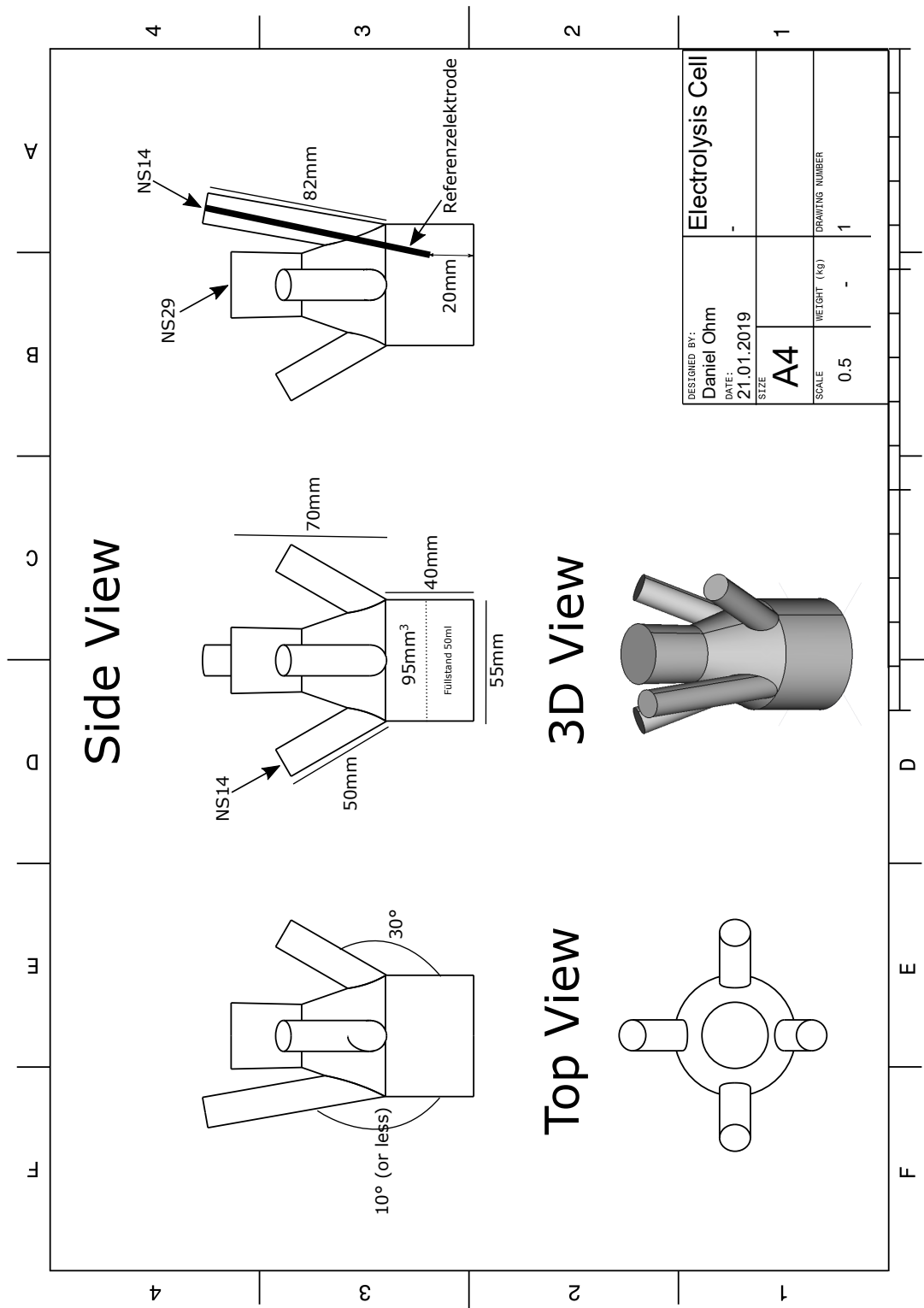


**Fig. 6.27:** (left) XPS spectrum (0 - 100 eV binding energy) of Ir/Au(111) showing signals for Ir. (right) XPS spectrum (900 - 960 eV binding energy) of Ir/Au(111). The spectrum shows no residues of copper left from CuUPD.

## 6.4 Electrochemical cell design



# List of Figures

2.1	Atom arrangement in the (100), (11) and (111) planes. . . . .	3
2.2	Defects on atomic scale of an aMoS <sub>2</sub> surface. High resolution STM images of local depressions (a), local contrast (b) and S-vacancies (c) on the surface. <sup>[11]</sup>	4
2.3	Schematics of the surface defects of single crystals. <sup>[14]</sup> . . . . .	5
2.4	Schematics of an electrochemical cell using a three-electrode setup. <sup>[21]</sup> . .	5
2.5	STM image (570 nm × 570 nm) of Au(111) partially covered with Pd, obtained at 0.25 V in 0.1 M H <sub>2</sub> SO <sub>4</sub> , after deposition of four monolayer equivalents of Pd at 0.4 V. <sup>[22]</sup> . . . . .	6
2.6	Redox reaction that happens at the substrate surface during the displacement reaction. . . . .	7
2.7	Schematics of the electrochemical displacement of one metal by another more noble metal. <sup>[26]</sup> . . . . .	7
2.8	Activity of different bulk metals to catalyze the ORR. <sup>[29]</sup> . . . . .	8
2.9	Relation between thickness of a Pt-layer and the resulting material costs. <sup>[5]</sup>	9
2.10	(a): Schematics of the TERS principle with a gold tip that gets illuminated by a laser source being close to the sample surface. <sup>[41]</sup> (b): EC-STM image of a Pd/Au-surface. <sup>[41]</sup> (c): Potential-dependent Raman-spectras recorded using EC-TERS. <sup>[42]</sup> . . . . .	11
3.1	Cyclic voltammograms of an Au(111) (black) in comparison to a non-commercial gold/glass sample (red). Recorded in 0.1 M H <sub>2</sub> SO <sub>4</sub> with a scan rate of 25 mV/s. (a): CV range 0.3 V to 1.1 V vs. SHE with signals for sulphate adsorption (broad signal) and order-/disorder-transition at 1.05 V vs. SHE. (b): CV range from 0.8 V to 1.7 V vs. SHE with signals for defect- and terrace oxidation (1.4 V and 1.6 V vs. SHE) and gold reduction (1.13 V vs. SHE). . . . .	13
3.2	STM image of the surface of a tested non-commercial gold-on-glass sample recorded with a Pt/Ir (80:20) tip at a scan speed of 1 line/s over a scan-range of 250 nm x 250 nm. . . . .	14

3.3	STM image of the surface of a Au(111) single crystal recorded with a Pt/Ir (80:20) tip at a scan speed of 1 line/s over a scan range of 250 nm x 250 nm.	15
3.4	Cyclic voltammogram recorded in 0.1 M H <sub>2</sub> SO <sub>4</sub> /1 mM CuSO <sub>4</sub> at an immersion potential of 0.72 V vs. SHE with an Au(111) bead single crystal as WE, a gold wire CE and a copper wire RE. The red and green lines indicate the potentials chosen for UPD experiments.	16
3.5	Current density-time trace recorded during CuUPD on gold-on-glass. Parameters: 0.44 V vs SHE, 3 s deposition time. The immersion potential of 0.72 V vs SHE was held for 23.5 s before the CuUPD potential was applied. The integration area for surface coverage calculation is highlighted in gray.	17
3.6	Correlation between surface coverage as function of deposition time and deposition potential.	18
3.7	STM images of a clean Au(111) sample (a) and of an Ir/Au(111) sample (b) and the average height profile of the Au step edge extracted from 5 individual height profiles of Au step edges (c) and the average height profile of Ir islands from individual height profiles of 10 islands (d).	20
3.8	Cyclic voltammogram of a clean Au(111) sample in comparison to the same sample after Ir was deposited on the sample surface. The inset shows the same CV cut at 0.2 V vs SHE to show the HER onset.	20
3.9	(a) STM image of a Pd/Au(111) sample after CuUPD and Pd displacement procedure. (b) Average height profile of the Pd islands.	21
3.10	Cyclic voltammogram of a clean Au(111) sample (black) in comparison to the same sample after CuUPD and Pd displacement procedure (green). The inset shows the region highlighted in grey.	22
3.11	STM images of Pd/Au(111). (a) Deposition potential 0.47 V vs. SHE (b) deposition potential 0.44 V vs. SHE, at 6 seconds deposition time.	22
3.12	Correlation between the size of the Pd islands and deposition time of copper on Au(111) at different deposition potentials.	24
3.13	STM images of gold surfaces with Pd (a) and Ir islands (b) CuUPD potential 0.47 V vs. SHE, 6 seconds deposition time.	25
3.14	Cyclic voltammogram of a Pd/Au(111) sample in the range of -0.2 V to 0.5 V vs SHE over 50 cycles at 25 mV/s scan rate with an immersion potential of 0.3 V vs SHE.	26
3.15	Cyclic voltammogram of a Ir/Au(111) sample in the range of -0.2 V to 0.5 V vs SHE over 50 cycles at 25 mV/s scan rate with an immersion potential of 0.3 V vs SHE.	27

3.16	Cyclic voltammogram of a Pd/Au(111) sample with different upper limit, starting with an upper limit of 0.6 V vs SHE up to an upper limit of 1 V vs SHE. . . . .	28
3.17	Cyclic voltammogram of a clean Au(111) sample in comparison Ir/Au(111) (a) and Pd/Au(111) (b) in the range of -0.2 V to 0.5 V vs SHE. Immersion potential: 0.3 V vs SHE, scan rate 25 mV/s in 0.1 M H <sub>2</sub> SO <sub>4</sub> . . . . .	30
3.18	Cyclic voltammograms of Pd/Au(111) (green) and Ir/Au(111) (red) compared to Au(111) (black) in the range of -0.2 V to 0.5 V vs SHE. Immersion potential: 0.3 V vs SHE, scan rate 25 mV/s in 0.1 M H <sub>2</sub> SO <sub>4</sub> . . . . .	30
3.19	Dependence of HER charge of Pd/Au(111) (a) and Ir/Au(111) (b) on deposition time. . . . .	32
3.20	Cyclic voltammogram of Pd/Au(111) in 0.1 M H <sub>2</sub> SO <sub>4</sub> and 0.1 M formic acid. Scan rate 20 mV/s, range 0.06 V to 0.7 V vs RHE. Blue line: CV of Pd/Au(111) before de poisoning procedure. . . . .	33
3.21	Anodic scan of Pd/Au(111) in 0.1 M H <sub>2</sub> SO <sub>4</sub> and 0.1 M formic acid, followed by a potential jump from 1.1 V down to 0.15 V. Scan rate 20 mV/s, range 0.15 V to 1.1 V vs RHE. . . . .	34
3.22	Areas under peak1 (black) and peak2 (red) after different number of linear sweep voltammetry cycles. . . . .	35
3.23	CV of pristine Au(111) (black) compared to Pd/Au(111) (green). Scan rate: 25mV/s in 0.1 M H <sub>2</sub> SO <sub>4</sub> and 0.1 M formic acid. . . . .	36
3.24	Cyclic voltammogram of Pd/Au(111) (a) and Ir/Au(111) (b) in 0.1 M H <sub>2</sub> SO <sub>4</sub> saturated with O <sub>2</sub> (Pd/Au(111) green, Ir/Au(111) red) and in O <sub>2</sub> -free degassed electrolyte (black). Scan rate 20 mV/s, range 0.06 V to 0.75 V vs RHE. . . . .	37
3.25	Cyclic voltammogram of Pd/Au(111) (green) and Ir/Au(111) (red) in 0.1 M H <sub>2</sub> SO <sub>4</sub> saturated with O <sub>2</sub> . Scan rate 20 mV/s, range 0.06 V to 0.75 V vs RHE. . . . .	38
3.26	ORR activity plotted against Cu deposition time for Pd/Au(111) (a) and Ir/Au(111) (b). The red marks are results that were excluded from the fit. . . . .	39
4.1	TER spectrum of Au(111) recorded at 1.4 V vs Pd-H in 0.1 M H <sub>2</sub> SO <sub>4</sub> with 5 s aquisition time, 7.92 mW at 632.8 nm excitation wavelength. . . . .	41
4.2	EC-STM image of Au(111) recorded at 1.4 V vs Pd-H in 0.1 M H <sub>2</sub> SO <sub>4</sub> , scan speed: 1 ln/s, setpoint: 1 nA. . . . .	42
4.3	Schematics of a future EC-TERS experiment to observe CO ad-/desorption on Pd/Au(111) during formic acid oxidation under potential control. . . . .	42

5.1	(a) Teflon tape prepared for use with the gold slides. (b) Gold sample prepared for the use in the experiments. . . . .	44
5.2	Electrochemical cell used for CV experiments for characterizations. . . . .	46
5.3	Scheme of the EC-TERS setup used in the experiments. Red: Incident beam path. Orange: Detection beam path. <sup>[58]</sup> . . . . .	49
5.4	Left: Image of the TERS cell used for the experiments mounted in the setup. Right: scheme of the TERS cell used in the experiments. <sup>[58]</sup> . . . . .	50
6.1	(left) CV of pristine Au(111). (right) CuUPD of Pd/Au(111) (3 s CuUPD deposition time, scanned from 0.4 V to 0.15 V vs Cu/Cu <sup>2+</sup> CuUPD deposition potential). . . . .	54
6.2	(left) STM image of Pd/Au(111) after CuUPD 3 s scan from 0.4 V to 0.15 V. (right) Average Pd island size. . . . .	54
6.3	(left) CV of pristine Au(111). (right) CV of Pd/Au(111) (3 s CuUPD deposition time, 0.12 V vs Cu/Cu <sup>2+</sup> CuUPD deposition potential). Immersion potential: 0.3 V vs SHE, scan rate: 25 mV/s. . . . .	55
6.4	STM image of Pd/Au(111) after CuUPD 3 s deposition time with 0.12 V deposition potential. . . . .	55
6.5	(left) CV of pristine Au(111). (right) CV of Pd/Au(111) (5 s CuUPD deposition time, 0.15 V vs Cu/Cu <sup>2+</sup> CuUPD deposition potential). Immersion potential: 0.3 V vs SHE, scan rate: 25 mV/s. . . . .	56
6.6	(left) STM image of Pd/Au(111) after CuUPD 5 s deposition time with 0.15 V deposition potential. (right) Average Pd island size. . . . .	56
6.7	(left) CV of pristine Au(111). (right) CV of Pd/Au(111) (9 s CuUPD deposition time, 0.15 V vs Cu/Cu <sup>2+</sup> CuUPD deposition potential). Immersion potential: 0.3 V vs SHE, scan rate: 25 mV/s. . . . .	57
6.8	STM image of Pd/Au(111) after CuUPD 9 s deposition time with 0.15 V deposition potential. . . . .	57
6.9	(left) CV of pristine Au(111). (right) CV of Pd/Au(111) (10 s CuUPD deposition time, 0.15 V vs Cu/Cu <sup>2+</sup> CuUPD deposition potential). Immersion potential: 0.3 V vs SHE, scan rate: 25 mV/s. . . . .	58
6.10	STM image of Pd/Au(111) after CuUPD 10 s deposition time with 0.15 V deposition potential. . . . .	58
6.11	(left) CV of pristine Au(111). (right) CV of Ir/Au(111) (3 s CuUPD deposition time, 0.15 V vs Cu/Cu <sup>2+</sup> CuUPD deposition potential). Immersion potential: 0.3 V vs SHE, scan rate: 25 mV/s. . . . .	59

6.12	STM image of Ir/Au(111) after CuUPD 3 s deposition time with 0.15 V deposition potential. . . . .	59
6.13	(left) CV of pristine Au(111). (right) CV of Ir/Au(111) (6 s CuUPD deposition time, 0.15 V vs Cu/Cu <sup>2+</sup> CuUPD deposition potential). Immersion potential: 0.3 V vs SHE, scan rate: 25 mV/s. . . . .	60
6.14	(left) STM image of pristine Au(111). (right) STM image of Ir/Au(111) after CuUPD 6 s deposition time with 0.15 V deposition potential. Immersion potential: 0.3 V vs SHE, scan rate: 25 mV/s. . . . .	60
6.15	(left) STM image Ir/Au(111). (right) Average Ir island size. . . . .	61
6.16	(left) CV of pristine Au(111). (right) CV of Ir/Au(111) (9 s CuUPD deposition time, 0.15 V vs Cu/Cu <sup>2+</sup> CuUPD deposition potential). Immersion potential: 0.3 V vs SHE, scan rate: 25 mV/s. . . . .	62
6.17	STM image of Ir/Au(111) after CuUPD 9 s deposition time with 0.15 V deposition potential. . . . .	62
6.18	(left) CV of pristine Au(111). (right) CV of Ir/Au(111) (12 s CuUPD deposition time, 0.15 V vs Cu/Cu <sup>2+</sup> CuUPD deposition potential). Immersion potential: 0.3 V vs SHE, scan rate: 25 mV/s. . . . .	63
6.19	(left) STM image of Ir/Au(111) after CuUPD 12 s deposition time with 0.15 V deposition potential. (right) Average Ir island size. . . . .	63
6.20	Full range (0 - 1200 eV binding energy) XPS spectrum of Pd/Au(111). . .	64
6.21	(left) XPS spectrum (45 - 75 eV binding energy) of Pd/Au(111). (right) XPS spectrum (70 - 95 eV binding energy) of Pd/Au(111). . . . .	64
6.22	(left) XPS spectrum (270 - 300 eV binding energy) of Pd/Au(111). The spectrum shows only low counts for carbon on the sample. (right) XPS spectrum (320 - 350 eV binding energy) of Pd/Au(111). . . . .	65
6.23	(left) XPS spectrum (650 - 710 eV binding energy) of Pd/Au(111). (right) XPS spectrum (900 - 960 eV binding energy) of Pd/Au(111). The spectrum shows no residues of copper left from CuUPD. . . . .	65
6.24	Full range (0 - 1200 eV binding energy) XPS spectrum of Ir/Au(111). . . .	66
6.25	(left) XPS spectrum (48 - 74 eV binding energy) of Ir/Au(111) showing signals for iridium. (right) XPS spectrum (74 - 94 eV binding energy) of Ir/Au(111). . . . .	66
6.26	(left) XPS spectrum (270 - 300 eV binding energy) of Ir/Au(111). The spectrum shows only low counts for carbon on the sample. (right) XPS spectrum (320 - 350 eV binding energy) of Ir/Au(111). . . . .	67

6.27 (left) XPS spectrum (0 - 100 eV binding energy) of Ir/Au(111) showing signals for Ir. (right) XPS spectrum (900 - 960 eV binding energy) of Ir/Au(111). The spectrum shows no residues of copper left from CuUPD. . 67

# List of Tables

3.1	Integrated signals for order-/disorder-transition, defect- and terrace-oxidation of the tested samples normalized to the signal of the Au(111)-single-crystal and the respective terrace-to-defect-oxidation ratio. . . . .	13
3.2	Surface coverage calculated from current vs time traces measured at two deposition potentials and different deposition times. . . . .	19
3.3	Ir island sizes depending on different deposition potentials and deposition times. . . . .	23
3.4	Pd island sizes depending on different deposition potentials and deposition times. . . . .	23
3.5	HER charge for different Pd/Au(111) samples in dependence of deposition time, island size and surface coverage. . . . .	31
3.6	HER charge for different Ir/Au(111) samples in dependence of deposition time, island size and surface coverage. . . . .	32
3.7	Formic acid oxidation charge and peak positions after multiple linear sweep voltammetries. . . . .	35
5.1	Properties of the non-commercial gold-on-glass samples. . . . .	44